FISEVIER

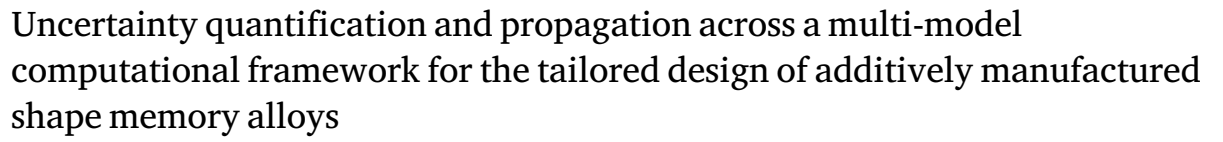
Contents lists available at ScienceDirect

Additive Manufacturing

journal homepage: www.elsevier.com/locate/addma



Full length article



Meelad Ranaiefar ^{a,*}, Pejman Honarmandi ^a, Jiahui Ye ^b, Chen Zhang ^b, Lei Xue ^a, Alaa Elwany ^b, Ibrahim Karaman ^a, Edwin J. Schwalbach ^c, Raymundo Arróyave ^{a,b,d}

- ^a Department of Materials Science and Engineering, Texas A&M University, College Station, TX 77843, United States
- b Wm Michael Barnes '64 Department of Industrial and Systems Engineering, Texas A&M University, College Station, TX 77843, United States
- c Materials and Manufacturing Directorate, Air Force Research Laboratory, Wright-Patterson Air Force Base, OH 45433, United States
- d J. Mike Walker'66 Department of Mechanical Engineering, Texas A&M University, College Station, TX 77843, United States

ARTICLE INFO

Keywords: ICME Uncertainty quantification Markov Chain Monte Carlo Bayesian calibration NiTiHf shape memory alloys Differential evaporation

ABSTRACT

Integrated computational materials engineering (ICME) combines the utility and efficiency of simulations with experimentation to drive forward materials design and discovery. These physics-based and data-driven frameworks have enabled material advancement by querying the complex process-structure-property-performance relationships to inform and guide experiments for the cost-effective design of alloy systems. In this study, a proven computational framework is presented and applied towards the tailored design of additively manufactured (AM) high-temperature NiTiHf shape-memory alloy (SMA) parts. Specifically, the effort deploys a design tool to attain specific transformation temperatures by composition control through differential evaporation, which in turn depends on processing conditions. This framework consists of a fast-acting discrete source model to simulate thermal history, a multi-layer model to account for composition evolution across melt pools, and a differential evaporation model to evaluate Nickel loss throughout the fabrication process. Besides the development of this multi-model chain, proper quantification of model uncertainties is critical to an ICME approach for materials design. Addressing these concerns, the parameter calibration and uncertainty quantification (UQ) of hierarchical model components is conducted through a Markov Chain Monte Carlo (MCMC) Bayesian approach over either the model itself or a representative Gaussian process-based surrogate model. These uncertainties are propagated across the models to the final response, i.e., martensitic start temperature. Subsequently, the hierarchical model framework is validated by comparing the experimental results with the most plausible values and uncertainty bounds obtained for the multi-model predictions at different processing conditions. From this calibrated and validated framework, process maps to streamline and illustrate the tailored design of AM high-temperature NiTiHf SMAs are developed, which demonstrates a promising path towards efficient design under uncertainty in additive manufacturing processes.

1. Introduction

Beyond the original and well-proven capabilities of Additive Manufacturing (AM) processes, such as geometric freedom and mass customization, a fast emerging avenue of development involves AM of functional materials such as NiTi-based alloys, with variations of the ternary component including Pt, Pd, Au, Zr, and Hf [1,2]. These shape

memory alloys (SMAs) exhibit a functional response based on temperature, where the ternary alloying element affects material properties such as hardness, superelasticity, and transformation temperature. NiTi, prominently known for its biocompatibility, and functional and mechanical properties, exhibits a martensitic start transformation temperature, M_s , spanning 100 °C for a composition range of (50–51) Ni at% [3]. However, NiTi SMA is limited in its use for high-temperature (HT) applications due to a low ceiling for M_s , approximately 70 °C. For

^{*} Correspondence to: NASA Glenn Research Center, Cleveland, OH 44135, United States.

E-mail addresses: meelad.ranaiefar@nasa.gov (M. Ranaiefar), hona107@tamu.edu (P. Honarmandi), jhy@tamu.edu (J. Ye), chenzhang@tamu.edu (C. Zhang), leixue11@tamu.edu (L. Xue), elwany@tamu.edu (A. Elwany), ikaraman@tamu.edu (I. Karaman), edwin.schwalbach@afresearchlab.com (E.J. Schwalbach), rarroyave@tamu.edu (R. Arróyave).

Nomenclature	
α	Shape parameter
$\alpha_{i,Ni}$	Activity (species i, Nickel)
\bar{p}	Equilibrium vapor pressure
ϕ	System hyperparameters, $\phi = \{S, \psi, \sigma_{\epsilon}^2\}$
Ψ	Kernel hyperparameters
θ	Vectors of calibration parameters
χ_{Ni}	Nickel content
Δt	Source discretization time scale
δ	Model discrepancy term
m ^{in,out,evap}	Mass flow relative to the melt pool (in, out, evaporation)
ℓ	Scale hyperparameter in kernel function
η	Efficiency
η_s	Surrogate function
ŝ	Volumetric energy source
κ	Thermal conductivity
β	Linear coefficient
Σ	Variance matrix of d
D	Observed data
d	Full data vector, $\mathbf{d} = (\mathbf{y}^{T}, \mathbf{z}^{T})^{T}$
H	Weight matrix
 h	Weight vector
I.	Prior information
t	Variance matrix
$\mathbf{t}_{ heta}$	Calibration inputs
\mathbf{W}	Weighted variance matrix
x	Control inputs vector
	New control inputs vector
$oldsymbol{x}_0 \ oldsymbol{\mathcal{X}}$	Parameter space of control inputs
v	Matérn smoothness parameter
ω	Weight fraction
	Density
ρ	Pearson correlation coefficient of predicted
ρ_{M_s}	and measured M_s
$ ho_{XY}$	Pearson correlation coefficient of parameter X and Y
σ	Standard deviation
σ^2	Variance term
σ_b	Beam size
σ_{ϵ}^2	Variance of observation error
$ au_i$	Time of source activation
Θ	Parameter space of calibration parameters
Θ_H	Heaviside step function
v	Velocity
\vec{r}	Vector of spatial coordinates (x_s, y_s, z_s)
A_A, B_A, C_A	Antoine coefficients
A_A, B_A, C_A A_{x-s}	Cross-sectional area
C	Correction factor
	Covariance function
c C	Specific heat capacity
C_p	
cov_{XY}	Covariance of parameter X and Y
d	Depth of melt pool

this purpose, tertiary SMA NiTiHf enables the cost-effective application of functional materials in high-temperature environments, exhibiting transformation temperatures dependent on both Ni and Hf content and an M_s ceiling exceeding 500 °C [4,5]. Umale et al. [6] demonstrate this

D_1	Inputs of simulation data \mathbf{y}^{\intercal}				
$D_2(\boldsymbol{\theta})$	Inputs of D_2 with vectors of calibration				
	parameters				
D_2	Inputs of experimental data \mathbf{z}^{\intercal}				
d_k	Keyhole depth				
D_t	Thermal diffusivity				
e	Observation error				
h_s	Hatch spacing				
j	Evaporation flux				
L	Length				
L_t	Layer thickness				
M	Molecular weight				
m	Mean function				
M_{s}	Martensite start transformation temperature				
P	Laser power				
p	Probability density function				
p_i°	Standard vapor pressure				
R	Distance between spatial position and heat				
	source				
R^2	Coefficient of determination				
r_{kh}	Keyhole radius				
S	Scaling parameter				
S_{iso}	Surface area of isotherm				
$T_{0,b,abs,iso}$	Temperature (initial, boil, absolute,				
* 0,b,abs,iso	isotherm)				
$t_{p,solid,melt}$	Time (process, solidification, melt)				
w	Width of melt pool				
y	Simulation output				
z.	Experimental observation				
AM	Additive manufacturing				
CI	Credible interval				
DEM	Differential evaporation model				
DSC	Differential scanning calorimeter				
DSM	Discrete source model				
EDM	Electrical discharge machining				
GP	Gaussian process				
HT	•				
	High temperature				
ICME	Integrated computational materials engi-				
ICP-AES	neering Inductively coupled plasma atomic emission				
ICF-AEO	spectroscopy				
КОН	Kennedy and O'Hagan framework				
LED	Linear energy density				
	Laser powder bed fusion				
LPBF					
MAP	Maximum a posterior probability				
MAPE	Mean absolute percentage error				
MCMC	Markov Chain Monte Carlo				
MH	Metropolis-Hastings				
MLM	Multi-layer model				
OM	Optical microscopy				
PDF	Posterior density function				
PSPP	Process-structure-property-performance				
RMSE	Root mean squared error				
SHT	Solution heat-treated				
SMA	Shape memory alloy				
UP	Uncertainty propagation				

NiTiHf composition-property relationship by varying Ni and Hf content between (49.8–51.3) at% and (0–30) at% respectively, resulting in an M_s range of nearly 700 °C, from -163 to 519 °C.

UO Uncertainty quantification VED Volumetric energy density

WDS Wavelength dispersive spectroscopy

Of crucial importance for the tailored design of AM-fabricated Ni-TiHf HT-SMA across this window of transformation temperatures is the knowledge of underlying physics and mechanisms to control processstructure-property-performance (PSPP) relationships. During the laser powder bed fusion AM (LPBF), a material undergoes multiple bouts of rapid solidification and cooling. The magnitude and duration of these events at a specific location depend on a combination of process parameters, including laser power, laser velocity, hatch spacing, etc. These parameters directly relate to melt pool geometry and the loss of alloying elements due to differential evaporation, resulting in location-specific composition throughout an AM part [7,8]. For NiTi alloys, a significant difference in volatility between alloying elements is conducive to significant changes in composition and properties through Ni loss and a sensitive Ni-M_s correlation [3]. Additively manufactured NiTiHf SMA shares this difference in volatility between alloying elements, allowing for quantifiable composition change due to differential evaporation [6, 8]. Informed modulation of AM process parameters then enables controlled modification of melt pool structure and composition change due to evaporation, corresponding to tailored changes in properties and fit-for-purpose components. However, this is not easily achieved and requires effective leveraging of simulations and experiments along the PSPP chain of integrated computational materials engineering (ICME) shown in Fig. 1.

Generally, the development of models and simulations is a vital task in the ICME framework to direct experiments in materials and product design along the PSPP chain. However, design is not viable without the calibration and uncertainty quantification (UQ) of these computational tools. These needs arise from our lack of knowledge about the physical systems, applied assumptions and simplifications, and incomplete parameterization [9]. In other words, UQ is necessary in order to provide a notion of confidence in computational-guided design. This necessity is especially prominent in AM process design due to the many complex physical phenomena and hard-to-measure variables involved, which correspond to multiple assumptions, missing physics, and lack of parameter knowledge in the relevant models and simulations. In the recent decade, Markov Chain Monte Carlo (MCMC) approaches in the context of the Bayesian inference have been commonly used to perform model calibration and UQ in different materials science and engineering problems [7,10-22]. The popularity of these UQ approaches is driven by their simple implementation, powerful and rigorous analysis, consideration of prior knowledge, and capability of updating analysis results upon acquiring new data [9]. However, the high computational cost of these methods restricts their application in the UQ of expensive models and simulations. In these cases, a surrogate-based MCMC technique, such as Kennedy and O'Hagan's Gaussian process (GP)-based approach [23] can be applied to quantify uncertainties [24,25].

In this work, a fast-acting ICME framework [7], consisting of a thermal model, multi-layer model, and differential evaporation model. is developed to achieve designable and controllable location-specific actuation in additively manufactured NiTiHf SMA components. For the purpose of accelerated materials design and discovery, the capabilities and speed alotted by this fast-acting framework serve as a swift tool ideal for screening PSPP trends. This is in contrast to high-fidelity models, e.g., finite element models, that require a high computational cost not suitable for expedited material development in the large and complex design space provided by AM. Additionally, the difficulties and costs associated with the calibration of high-fidelity models further hinder their application in the ICME materials design. However, to fill the

accuracy gap resulting from the reduction of considered physics in lowfidelity models, probabilistic calibration approaches are applied over the fast-acting low-fidelity models in this framework to identify the uncertainty bounds of the final model outcomes, i.e., location-specific properties of additively manufactured parts, sufficient to provide a notion of robustness in materials design.

The current work seeks to develop a framework for the robust design of additively manufactured NiTiHf. By quantifying the overall uncertainty, obtained from the contribution of individual model parameters, the framework can then be leveraged for design. In this regard, the calibration process and uncertainty quantification are performed using an MCMC Bayesian approach directly over the thermal model component and indirectly over the differential evaporation model through a representative Gaussian process-based surrogate model. Following this, quantified uncertainties are propagated across the modeling framework to the final model response, martensitic start temperature. Subsequently, the hierarchical model framework is validated through comparing the experimental results with the most plausible values and uncertainty bounds obtained for the multi-model predictions at different processing conditions. Exploiting this calibrated and validated computational framework, process maps are developed for the sake of tailored design of additively manufactured high-temperature Ni-TiHf SMAs, providing a promising path towards efficient design under uncertainty in AM processes.

2. Material response during the thermal process

2.1. Thermal model

A discrete source model (DSM) proposed by Schwalbach et al. [26] is applied in this work to predict the thermal history and melt pool characteristics in a fast-acting manner during the thermal process of an AM part. While high-fidelity numerical simulations, such as finite difference, volume, or element, are required to precisely capture the physics in the AM thermal processes, their high computational cost makes them impractical for process design in the context of the ICME paradigm, particularly the processes involving forward-feeding and in-line feedback control. Therefore, the development of low-fidelity fast-acting analytical models with comparable precision is essential to a successful approach in tackling AM design problems.

2.1.1. Assumptions

The DSM enables fast-acting temperature predictions of AM parts by simulating thermal history while accounting for a series of key assumptions. These assumptions offer a balance between computational cost and accuracy. In this regard, the main considerations fall into the categories of thermophysical properties and heat transfer.

For the purpose of predicting AM melt pool characteristics, Schwalbach et al. [26] has quantified small differences resulting from material property temperature dependence. From this, temperature-independent thermophysical properties are thus assumed by the DSM in this work. Additionally, experiments are utilized in a probabilistic calibration of the model to provide effective thermophysical property values alongside the property's associated distributions. Uncertainties stemming from the temperature-independence assumptions are accounted for through the calibration procedure.

Heat transfer within the material system is directly governed by thermal conduction. Additionally, material absorption and thermal transport mechanisms including convection and radiation, as well as evaporation, are accounted for through a calibrated efficiency parameter. Considering the dependence of melt pool shape on convection, a shape factor variable to adjust the volumetric energy source and consequent melt pool geometry for a given set of process conditions can be tuned and calibrated [26]. However, a calibrated shape factor is not transferable to multiple process parameters within the same material system and will result in extensive computational cost when screening

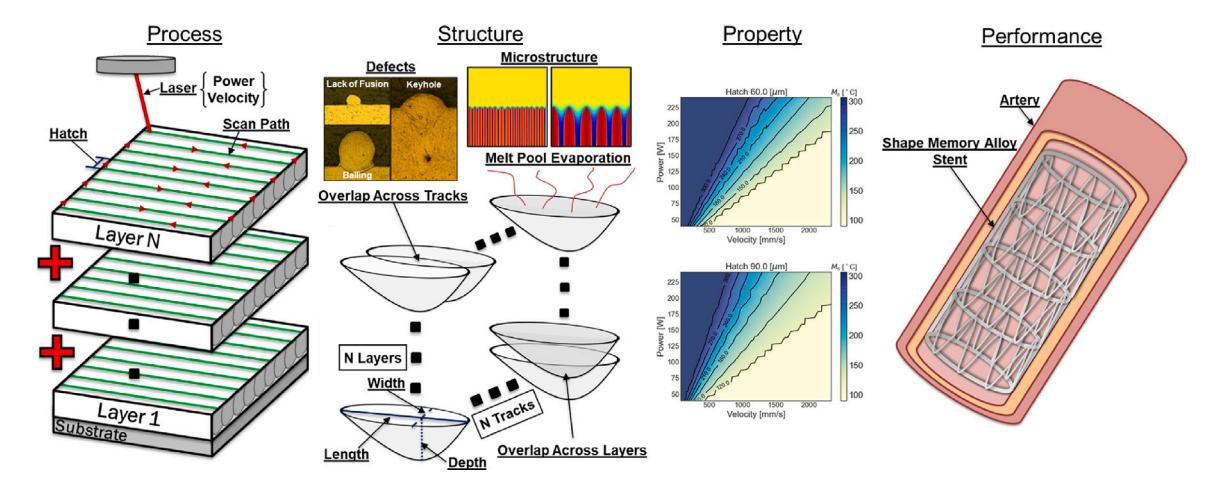


Fig. 1. Schematic of an integrated computational materials engineering modeling approach for LPBF AM. This is established through a process-structure-property-performance (PSPP) relationships.

for trends. For this reason, the shape factor is assumed to have a value equal to 1, but a generalized physics-based depth correction factor is considered [27] and calibrated with experiments for cases when the AM process is characterized by keyholing mode through a criterion derived from NiTiHf printability maps [8]. This presents significant disparities in melt pool width to depth ratios for the keyholing conditions due to substantial evaporation of material and corresponding recoil pressure [28].

In the context of heat transfer and temperature distribution of the melt pool, latent heat due to liquid–solid and solid-state phase change, as well as sensible heat, are also considered, subsumed by a calibrated effective heat capacity parameter. The calibration approach and results for the thermophysical properties, efficiency, and depth correction are discussed in Sections 2.3 and 2.4, respectively.

2.1.2. Thermal profile

The DSM predicts temperature, T, at any given spatial location along the x_s , y_s , and z_s coordinates, \vec{r}_j , over the AM process. These predictions at any given process time, t_p , provide isotherm contours that are used to determine the melt pool dimensions based on the material melting temperature. In this model, the temperature prediction is performed by solving the heat conduction equation in the presence of a series of volumetric discrete heat sources, $\{\hat{s}_i\}_{i=1}^N$, at designated locations, $\{\vec{r}_i\}_{i=1}^N$, which sequentially activate at different process times, $\{\vec{r}_i\}_{i=1}^N$, depending on the laser beam velocity, v. This equation is expressed as:

$$\frac{\partial T}{\partial t_p} = D_t \nabla^2 T + \sum_{i=1}^N \frac{\hat{s}_i(\vec{r}_j, t_p)}{\rho C_p} \tag{1}$$

where D_t , ρ , and C_p are the thermal diffusivity, mass density, and mass specific heat capacity of the given material, respectively. As mentioned in Section 2.1.1, these parameters are considered temperature-independent and represented by their effective quantities. It should also be noted that the thermal diffusivity can be related to the thermal conductivity, κ , as $D_t = \frac{\kappa}{\rho C_p}$. Assuming normally-distributed volumetric heat sources centered at \vec{r}_i with standard deviation, σ_b representing the beam size, the following solution based on Green's function technique can be derived from Eq. (1) for an infinite uniform medium assigned at initial temperature T_0 :

$$T(\vec{r}_{j}, t_{p}) = T_{0} + \sum_{i=1}^{N} \left\{ \frac{\eta_{i} P_{i} \Delta t}{\rho C_{p} \sqrt{2} \pi^{1.5}} \Theta_{H}(t_{p} - \tau_{i}) \left(\sigma_{b}^{2} + 2D(t_{p} - \tau_{i}) \right)^{-1.5} \right.$$

$$\left. \exp \left(-\frac{R_{ij}^{2}}{2 \left(\sigma_{b}^{2} + 2D_{t}(t_{p} - \tau_{i}) \right)} \right) \right\}$$
(2)

where η_i is an adjusting factor called efficiency, indicating the energy received by the material from the heat source \hat{s}_i . In other words, this factor accounts primarily for energy loss due to limited absorptivity, and secondarily for the energy loss due to convection, radiation, and evaporation phenomena in the final solution. While P_i is the power of heat source i, $\eta_i P_i$ is known as its effective power. η_i and P_i are considered fixed in this work and denoted by η and P. Δt is the source discretization timescale. $R_{ij} = |\vec{r}_j - \vec{r}_i|$ corresponds to the distance between the given spatial position and the position of the heat source \hat{s}_i . Θ_H is the Heaviside step function accounting for the contribution of heat sources activated at process time t_p . For further information about DSM, the readers are referred to [26].

2.1.3. Melt pool geometry

LPBF AM process parameters and material properties directly affect melt pool geometry and structure. For a given material, modulating laser power, laser speed, and hatch spacing translates to different energy inputs into the system and variations in melt pool geometry. Even within a single layer there is variation in location-specific energy, resulting in unique melting and solidification events throughout the AM process. Proper evaluation of these events at specific points in time then enables the approximation of corresponding melt pool geometries. By leveraging the DSM to simulate a desired print, melt pool geometries for any point in time and at any spatial location can be generated.

Resolving melt pool dimensions follows a short sequence beginning with the generation of an AM layer based on desired process parameters. Next, a specific point of interest on the simulated layer is chosen and the thermal history is generated. For the identification of a specific thermal event within the thermal history, an approximate range of times corresponding to the melting and solidification event should also be specified. The material's melt temperature is then used as a criterion to determine the start and end, respectively the melting and solidification time, of the thermal event. The melt pool width and depth are then determined by querying points for the solidification temperature in a radial vector search pattern originating from the location of interest, bounded by the timing of the thermal event. This results in a cross-section of queried points, where the thermal history of each point should be resolved to determine a respective duration of the thermal event, defined by the melting and solidification time. Under the steady-state assumption, the length for each point in the cross-section can then be calculated as a summation of its length before, L_B , and length after, L_F , the cross-section, as shown in Fig. 2. These lengths are based on the distance traveled by the laser relative to the solidification time of the cross-section boundary points, where length is zero, and both the solidification time and melting time of individual

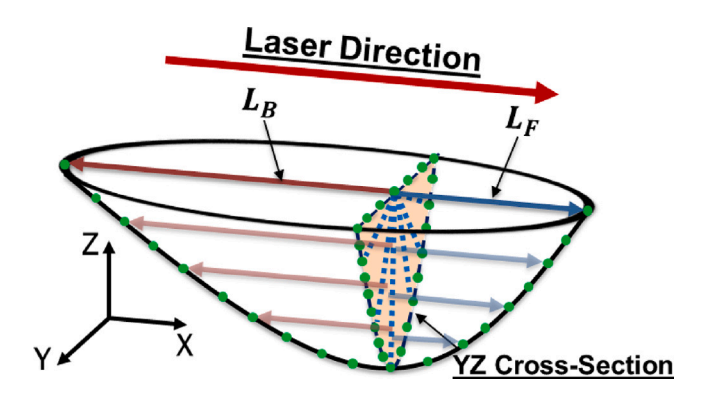


Fig. 2. Sample melt pool with queried points in the YZ cross-section. The melt pool length corresponding to any point in the cross-section is comprised of components for both the length before, L_B , and the length in front, L_F , of the cross-section.

points within the cross-section. The total length $L_{(y_s,z_s)}$ corresponding to a specific point in the cross-section can be solved as:

$$L_{(y_s, z_s)} = [L_B + L_F]v = [(t_{solid, (y_s, z_s)} - t_{solid, min}) + (t_{solid, min} - t_{melt, (y_s, z_s)})]v$$
 (3)

where $t_{solid,(y_s,z_s)}$ and $t_{melt,(y_s,z_s)}$ are the solidification and melting time of a point in the cross-section, respectively, $t_{solid,min}$ is the earliest solidification time from all points in the cross-section, and v is the laser velocity. By generating lengths for each point in the cross-section, an approximation of the 3D melt pool is resolved and a melt pool volume is determined. This is a critical component to calculating composition evolution through an AM part, discussed in Section 3.

2.1.4. Prediction correction for the keyhole depth

Keyholing is a common defect in the AM processes which occurs in high input energy processes resulting from specific combinations of high laser power and low laser velocity. In these conditions, materials' incapability of dissipating sufficient heat from the melt pool underneath the laser beam leads to a local increase in temperature above the materials boiling point, inducing massive elemental evaporation from the melt pool. Therefore, an evaporation-induced force, also known as the recoil pressure, is produced in an opposite direction perpendicular to the melt pool surface [7,10]. When the recoil pressure is larger than its opposing counterpart resulting from surface tension, it forms a vapor cavity by pushing out its inner molten material. This cavity promotes heat absorption and enables the laser beam to penetrate deeper than non-keyhole conditions [29].

Analytical thermal models, such as the model described in Section 2.1, typically ignore the physics involved in keyholing mode, resulting in melt pool depth underestimation at these conditions. For this reason, the same depth correction as our previous studies [7,10] is applied here for cases undergoing the keyholing phenomenon. This correction is taken into account using the simplified analytical model for the keyhole depth, d_k , suggested by Gladush and Smurov [27], which is derived by solving the heat conduction equation for a cylindrical-assumed keyhole of radius r_{kh} under the laser beam with a semi-infinite boundary condition. The final general solution is expressed in terms of the processing conditions, i.e., laser power, velocity, and beam size, as well as some materials properties, as follows:

$$d_k = \frac{\eta P}{2\pi\kappa T_b} \ln\left(\frac{r_{kh} + \frac{D}{\nu}}{r_{kh}}\right) \tag{4}$$

where \mathcal{T}_b is the material boiling temperature alongside other previously defined properties.

Assuming the depth prediction in Eq. (4) can perfectly represent the experimental data for keyhole depths, the discrepancy between the DSM prediction and experimental data is considered a constant fraction of this depth under the keyholing conditions. This constant fraction is called the correction factor, C, in our studies in order to account for keyholing missing physics in the DSM and calibrated probabilistically besides other uncertain model parameters against available experimental data for melt pool dimensions. The correction factor should change between 0 and 1 based on the high-precision assumption for Eq. (4). However, our previous studies [7,10] showed that it can be higher than 1 since the keyhole depth can still be underestimated by Eq. (4).

For the sake of parameter calibration, an experimentally-derived criterion is used to identify the processing conditions in the given data corresponding to the keyholing occurrence, at which the DSM depth predictions are required to be corrected. This criterion is expressed as an inequality between melt pool width, w_{exp} , and depth, d_{exp} , as $(w_{exp}/1.5) \leq d_{exp}$ for Ni-based SMAs, which corresponds to a classified P-v region in the printability maps for these alloys [30]. Therefore, the depth correction can also be performed based on a criterion for the combinatory values of P and v input into the thermal model.

2.2. Experimental procedure

Ni_{50.3}Ti_{29.7}Hf₂₀ (at.%) ingots were acquired from Ingpuls GmbH and then gas atomized by Nanoval GmbH & Co. KG. The atomized powder possessed a D80 (80th percentile of particle size distribution) of 41 µm and was utilized for single track and solid specimen fabrication throughout this study. Thin disks of the NiTiHf were cut by wire electrical discharge machining (wire-EDM) for printing NiTiHf single tracks. Fifty four single tracks with length of 10 mm and spacing of 1 mm were fabricated using DMP ProX 200 LPBF system by 3D Systems with different combinations of laser power and scanning speed under argon atmosphere. These print conditions, their linear energy density (LED), and their corresponding average values of melt pool width and depth are listed in Table 1. Additionally, these prints are split into training and test sets to calibrate and validate the thermal model parameters. It should be noted that melt pool width and depth are the only measurable quantities in this experimental setup, while melt pool length and thermal profiles must be predicted through the calibrated thermal model. Furthermore, the data is identical to that of Zhang et al. [8], which can be referenced for additional information on the experimental details.

After the single track experiments, top-view optical microscopy (OM) images were taken at the middle of each single track using a Keyence VH-X digital microscope, and the widths were measured and averaged at five different locations from the OM images. For each single track, three cross-sectional samples were cut using wire-EDM at equal-spaced distance. The cross-sectional samples were mechanically polished up to 1200 grit, followed by a final polishing with colloidal silica solution. In order to reveal the melt pool shapes, the polished samples were etched with the etchant (3 parts HNO₃, 1 part HF, 10 parts distilled water). OM was carried out on each etched cross-section to measure the melt pool depths, and the average of three cross-sectional samples was calculated for each single track. Fig. 3 contains cross-section images of these single-track prints for several processing conditions, characterizing differences in melt pool geometry for lack of fusion, good quality, balling, and keyholing print modes.

2.3. Probabilistic calibration approach

Computer models are always imperfect due to the incomplete parameterization and physical knowledge incorporated in these models [9]. Therefore, model calibration is required and should utilize a probabilistic approach in order to assess validity [31]. Bayesian inference is a simple and straightforward approach that applies the Bayes' theorem to identify the probability of the parameter quantities represented by a parameter posterior density function (PDF), given the observed data, \mathbf{D} , and parameter prior information, \mathbf{I} . Parameter posterior probability, $p(\theta|\mathbf{D},\mathbf{I})$, is proportional to the product of parameter prior probability, $p(\theta|\mathbf{I})$, and likelihood, $p(\mathbf{D}|\theta,\mathbf{I})$ in this context [32].

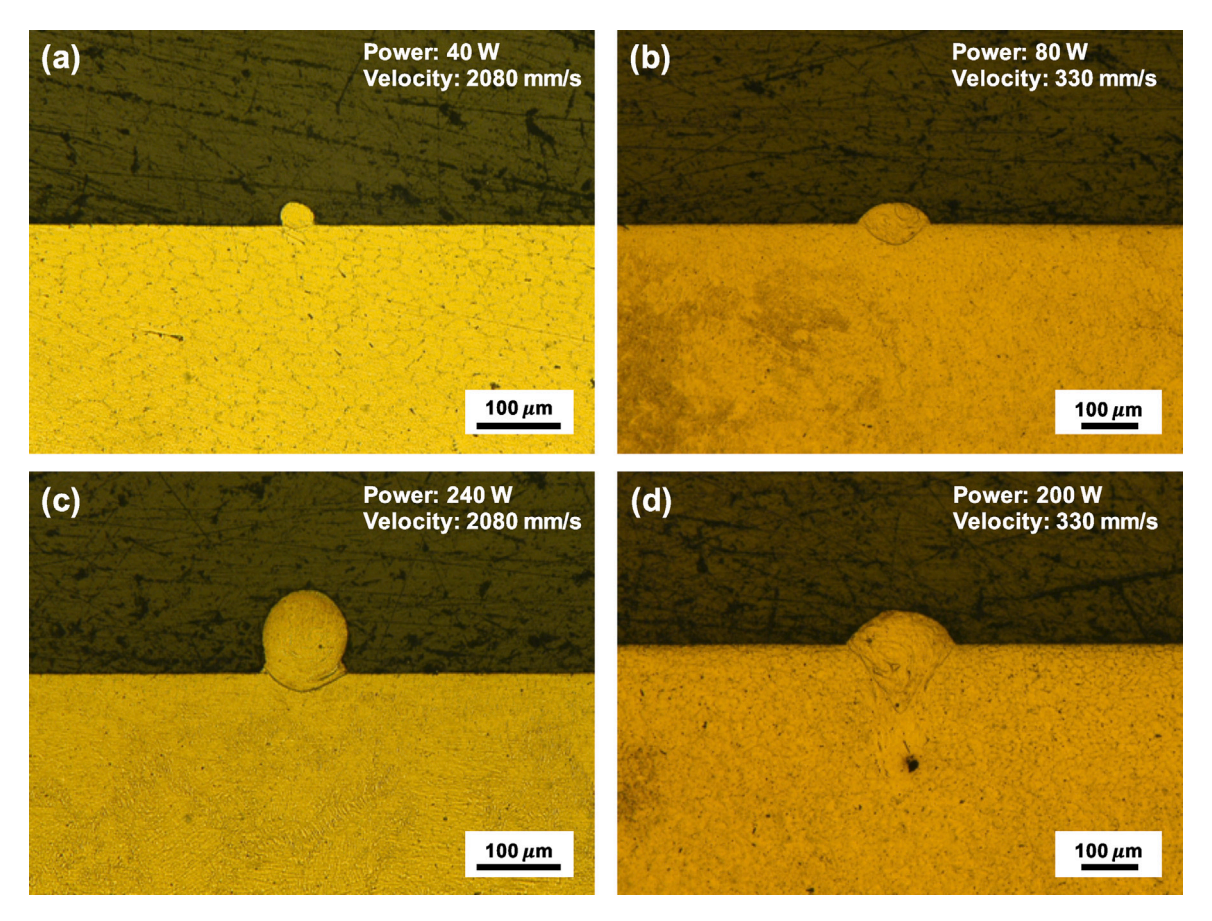


Fig. 3. Cross-section images for LPBF Ni_{50.3}Ti_{29.7}Hf₂₀ single-track prints obtained through optical microscopy. Based on print conditions, different print modes are experienced:
(a) lack of fusion (b) good quality (c) balling (d) keyboling.

However, this inference typically involves solving multi-dimensional intractable integrals to determine the posterior statistical characteristics. These integrations are difficult or often impossible to compute through the analytical and conventional numerical methods [9,33]. Markov Chain Monte Carlo sampling techniques are mostly used in order to tackle these integration problems in a robust and straightforward manner [34–36].

In this work, an MCMC toolbox in Matlab [37] based on the adaptive Metropolis-Hastings (MH) algorithm is employed to infer the posterior distribution of the model parameters. For this purpose, parameter vectors are sampled from this multivariate posterior distribution, iteratively, after defining the parameters' initial guess, bounds, and prior distribution. In each iteration of this process denoted by index i, a candidate, θ^{cand} , is sampled from a proposal posterior distribution, q. In the beginning, the proposal distribution is considered as a multivariate Gaussian proposal distribution centered at the parameters' initial guess with an arbitrary variance-covariance matrix. Then, it is adapted to a multivariate Gaussian distribution centered at the previous parameter vector, $\theta^{(i-1)}$, in the MCMC chain with a variance–covariance matrix calculated as a function of the variance-covariance matrix of all the previous parameter vectors in the chain, based on Haario et al.'s works [38,39]. The acceptance/rejection of the sampled candidate is performed based on the MH ratio that is:

$$MH = \frac{p(\boldsymbol{\theta}^{cand} | \mathbf{I}) p(\mathbf{D} | \boldsymbol{\theta}^{cand}, \mathbf{I})}{p(\boldsymbol{\theta}^{i-1} | \mathbf{I}) p(\mathbf{D} | \boldsymbol{\theta}^{i-1}, \mathbf{I})} \frac{q(\boldsymbol{\theta}^{i-1} | \boldsymbol{\theta}^{cand})}{q(\boldsymbol{\theta}^{cand} | \boldsymbol{\theta}^{i-1})}, \quad i = \{1, \dots, n\}$$
 (5)

where the first ratio is the Metropolis ratio expressed as the product of the prior probability of θ^{cand} and the likelihood of obtaining the observed data given this sample over its counterpart given $\theta^{(i-1)}$. In other words, the posterior probabilities of θ^{cand} and $\theta^{(i-1)}$ are compared through this ratio. It should be noted that the parameter prior

distribution is defined based on prior knowledge about the parameters. However, a non-informative distribution, e.g., uniform, is considered when no previous information is available. Moreover, likelihood is a multivariate Gaussian distribution in the applied MCMC toolbox, which compares a vector of the observed data at different input conditions with its corresponding vector of model outputs at any given theta. This multivariate Gaussian distribution is centered at the observed data vector with a diagonal variance—covariance matrix of data variances.

The second ratio in Eq. (5) is the Hastings ratio that compares the probability of moving forward from $\theta^{(i-1)}$ to θ^{cand} with its counterpart for the reverse move. The parameter vector candidate is accepted if the MH ratio is higher than a random value between 0 and 1. This is equivalent to an acceptance probability of $min\{MH, 1\}$ for the candidate. θ^i equals θ^{cand} in the case θ^{cand} is accepted; otherwise, θ^i is the same as $\theta^{(i-1)}$. The iterative sampling of parameter vectors continues until the proposal distribution becomes almost stationary, which is generally equivalent to parameter convergence in the MCMC process. Then, the parameter samples generated after the convergence can represent the parameter posterior PDF and its statistical properties for the sake of parameter calibration and uncertainty quantification. The model outputs at these parameter samples are used to find uncertainties propagated from the parameters to the model outputs. Moreover, 2.5% of the model output samples can be discarded from their upper and lower bounds to predict 95% credible intervals (CIs).

2.4. Calibration results

The DSM, similar to all models with any range of fidelity or precision, is incapable of emulating reality perfectly due to its assumptions, simplifications, and incomplete physics. Therefore, the quantification of existing errors is required in order to have a notion of confidence for the

Table 1 Average measured melt pool width and depth for single-track prints at different LPBF process conditions over $\mathrm{Ni}_{50.3}\mathrm{Ti}_{29.7}\mathrm{Hf}_{20}$ (at.%) powder. Experimental data selected for the calibration and validation of the thermal model are separated.

uiciillai i	nouer are separar	.cu.		
P [W]	v [mm/s]	LED [J/m]	$\bar{w} \ [\mu m]$	đ [μm]
Training	data for therma	l model calibratio	n	
40	80	500.0	126.9	21.4
80	80	1000.0	244.9	64.9
120	80	1500.0	385.6	235.3
160	80	2000.0	462.7	400.9
240	80	3000.0	551.2	721.8
40	330	121.2	83.1	9.4
80	330	242.4	116.4	42.3
120	330	363.6	173.6	129.7
160	330	484.8	206.6	222.5
200	330	606.1	227.7	247.3
80	580	137.9	97.2	32.4
120	580	206.9	125.0	63.4
200	580	344.8	165.9	100.8
240	580	413.8	173.6	112.3
80	830	96.4	78.7	11.6
120	830	144.6	113.2	42.3
160	830	192.8	137.8	71.3
200	830	241.0	142.9	72.8
240	830	289.2	157.0	144.1
80	1080	74.1	73.9	11.6
160	1080	148.1	113.5	57.0
240	1080	222.2	138.4	94.8
80	1330	60.2	74.6	6.8
120	1330	90.2	80.6	17.8
160	1330	120.3	83.8	40.8
240	1330	180.5	109.4	78.3
160	1580	101.3	74.8	32.7
200	1580	126.6	79.0	49.3
120	1830	65.6	72.3	10.8
160	1830	87.4	66.8	27.4
240	1830	131.1	69.1	53.5
120	2080	57.7	68.5	7.6
160	2080	76.9	59.8	23.2
200	2080	96.2	59.5	34.2
240	2080	115.4	67.8	39.1
120	2330	51.5	69.8	8.7
160	2330	68.7	58.5	20.2
240	2330	103.0	68.7	43.8
60	205	292.7	101.0	16.8
100	205	487.8	181.9	51.8
140	205	682.9	248.4	183.5
100	455	219.8	109.0	35.4
140	455	307.7	162.4	71.5
Test dat	a for thermal mo	del validation		
200	80	2500.0	522.5	557.0
240	330	727.3	240.4	320.3
160	580	275.9	158.3	74.0
120	1080	111.1	84.4	28.1
200	1080	185.2	123.1	71.5
200	1330	150.4	94.0	55.5
120	1580	75.9	76.8	10.4
240	1580	151.9	75.5	63.4
200	1830	109.3	73.9	38.4
200	2330	85.8	63.9	26.9
60	455	131.7	77.8	9.5
-				

model predictions, enabling the application of such a model in design methodologies. For this purpose, the Bayesian MCMC inference method described in Section 2.3 is applied to perform the probabilistic calibration of the model parameters against the closest information source to reality, i.e., experimental data. Then, the parameter uncertainties are propagated to the model outputs in order to have predictions within uncertainty bounds at any given processing condition.

Out of 54 available experimental data points for melt pool width and depth presented in Table 1 at different processing conditions of printing $Ni_{50.3}Ti_{29.7}Hf_{20.0}$ SMA single-tracks, 43 data points (80%) are considered as training data for the probabilistic calibration and the

Table 2 The most plausible (mean) values and standard deviation of the DSM parameters after the MCMC calibration against the experimental data for $Ni_{50.3}Ti_{29.7}Hf_{20.0}$ SMA single-track melt pool dimensions.

η	κ [W/m K]	C _p [J/kg K]	С	
0.64 ± 0.08	13.22 ± 1.87	652.53 ± 76.38	0.81 ± 0.03	

rest (20%) are used as test data for the validation of the calibrated model. It should be noted that the Bayesian inference provides the best plausible results based on the current experimental information and is not impeded by the number of data points. However, this statistical inference can be updated when more data is available.

Using all the training experimental data points from both conduction and keyholing modes at the same time, the uncertain model parameters, i.e., η , k_{eff} , C_{p-eff} , and C, are probabilistically calibrated through the MCMC sampling approach in a multi-objective optimization scheme. This process starts by considering appropriate ranges for parameters based on the physical constraints and expert intuition alongside a uniform prior distribution due to the lack of knowledge about the parameters' distribution form. Subsequently, 20,000 parameter vector samples are generated using the MH criterion discussed in Section 2.3. After discarding the burn-in period from the sample chain, the parameter vector samples represent a multivariate joint posterior probability density function (PDF) for the parameters that is illustrated through the marginal (individual) and bivariate (pair) joint parameter PDFs in Figs. 4 and 5, respectively. The statistical properties of the marginal PDFs that include the mean and standard deviation of samples for the individual parameters are reported in Table 2 as their calibrated values and uncertainties. Also, the pair joint PDFs that show the probability densities in the parameter pair spaces in different colors, increasing from blue to red, imply the extent of linear correlation between each parameter pair in a qualitative manner through the linearity of color features.

The Pearson correlation coefficient, $\rho_{XY} = cov(X,Y)/\sigma_X\sigma_Y$, provides a quantitative measure enabling the comparison of the linear correlations, where σ_X , σ_Y , and cov(X,Y) are the standard deviation of parameter X, the standard deviation of parameter Y, and the covariance of these two parameters, respectively. This quantitative parameter alters from -1 to 1. The upper and lower bounds correspond to a full linear correlation between the given parameter pair, contrarily 0 implies no linear correlation. Also, the negative and positive signs indicate the correlation direction, meaning whether the value of one of the pairs decreases or increases as the value of the other pair increases. As shown in the bottom right corner of plots in Fig. 5, there is almost a full linear correlation between η and $C_{\text{p-eff}}$ and fairly high correlations between η and k_{eff} as well as k_{eff} and $C_{\text{p-eff}}$. These correlations can also be observed in the marginal PDFs in Fig. 4. Part (c) of this figure shows that the $C_{\text{p-eff}}$ distribution peak falls beyond the lower bound of this parameter since the probability density increases as the $C_{p,eff}$ value approaches the lower bound. However, having a parameter value under its lower bound is physically unreasonable, which can result from assumptions and missing physics in the DSM or errors in the experimental results. As a result of a very high linear correlation between η and $C_{\text{p-eff}}$ (r = 0.99), Fig. 4-(a) also shows a very similar marginal PDF for η . However, as shown in Fig. 4-(b), the marginal PDF in the case of k_{eff} is less similar to the one for $C_{\mathrm{p-eff}}$ and mostly shows a double peak distribution as the linear correlation drops to 0.81. Fig. 5 also exhibits low linear correlations between C and the other three parameters, indicating C has an independent contribution to predictions and cannot be replaced by the mentioned model parameters. This independent behavior results in a clear peak in the marginal PDF of parameter C in Fig. 4-(d).

The most plausible values and uncertainties of the DSM parameters listed in Table 2 are propagated to the model outputs, i.e., melt pool width and depth, through the model forward analysis of the parameter

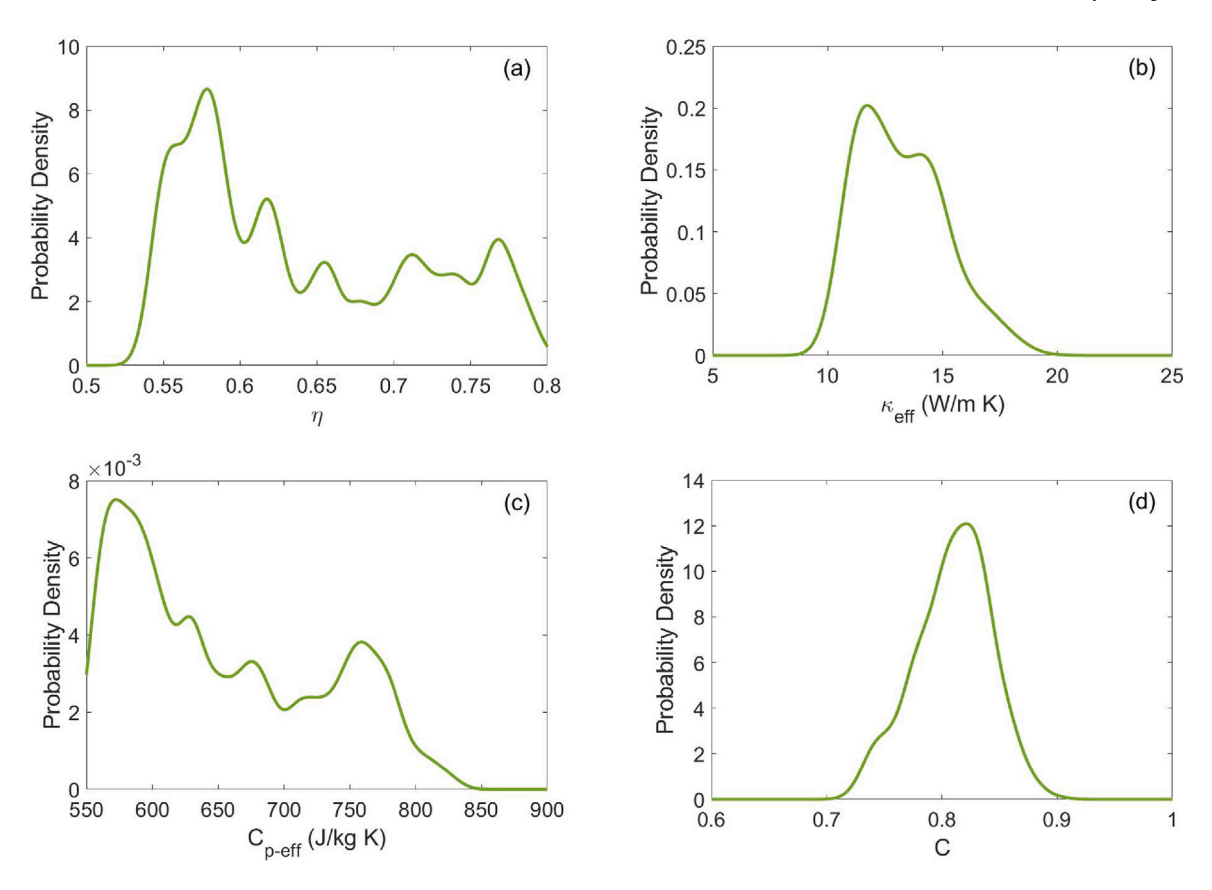


Fig. 4. Marginal posterior PDFs of the DSM parameters obtained after the MCMC calibration against the experimental data for Ni_{50.3}Ti_{29.7}Hf_{20.0} SMA single-track melt pool dimensions.

mean vector and the MCMC parameter vector samples after discarding the burn-in period. In this uncertainty propagation (UP) scheme, 2.5% of the output samples for melt pool width or depth are discarded from the upper and lower bounds of the sorted output samples in order to obtain 95% CIs at each experimental print condition. These probabilistic predictions versus their corresponding experimental data are plotted in Fig. 6 for both training (part (a) and (b)) and test (part (c) and (d)) experimental conditions. Colors in this figure represent the LED values at different print conditions. As observed in Fig. 6-(a) and (b), the predictions of the calibrated DSM model are in excellent agreement with their corresponding training data with R2 and RMSE values of 0.94 and 32 μm for melt pool width and 0.93 and 43 μm for melt pool depth. Comparable R^2 and RMSE values of 0.95 and 35 μm for melt pool width and 0.97 and 31 µm for melt pool depth for test-experimental conditions in Fig. 6-(c) and (d) also validate the calibration results with no over-fitting. Therefore, the calibrated DSM model is applied in our multi-model framework in Section 3 and Section 4 to predict melt pool overlap, evaporation flux, final composition, and transformation temperatures for different print conditions of cuboid specimen.

3. Composition evolution across melt pools

3.1. Multi-layer model

A multi-layer model (MLM) proposed by Ranaiefar et al. [7] is applied in this work to assess melt pool overlaps resulting from the AM process and to account for composition evolution across a part. The MLM is important for appropriately defining the PSPP chain of an AM part because it assists in accounting for the multiple thermal events and the associated evaporation of alloying elements which occur during the AM fabrication process. By simulating multiple layers within an AM part and the corresponding melt pool overlap and differential evaporation, the model framework takes an additional step towards becoming

a fast-acting 3D model, analog to a digital twin, ideal for screening PSPP trends. Additionally, the MLM receives melt pool geometry input directly from the calibrated DSM and does not require direct calibration as there are no uncertain parameters in this model. However, model uncertainty may be propagated from the DSM through the MLM and to the remainder of the model framework by utilizing the MCMC samples generated in Section 2.4 as input parameters, as demonstrated later in Section 5.1.

3.1.1. Assumptions

Simulating each of the hundreds to thousands of layers fabricated during the AM process is computationally expensive and impractical in the context of utilizing the model framework to screen for PSPP trends and accelerated development in design. For this reason, the MLM implements a series of assumptions to reduce computational cost for the simulation of multiple layers. In this regard, the main considerations fall into the categories of preheat effects and melt pool overlap.

During the AM process, there are both intralayer and interlayer preheating effects which impact melt pool dimensions. Intralayer preheating describes the diffusion and build-up of heat across a single layer. The influence of intralayer preheating on melt pool dimensions is highly dependent on the scan strategy and the part shape, where small hatch spacing and quick turn-arounds result in larger preheat temperatures in adjacent tracks relative to increased hatch spacing and delayed turn-around times. When a region with raised preheat temperature is processed, the thermal field at a point in time, defined by the melting temperature, would be larger than at a point with no or less thermal build-up. This intralayer preheating effect is inherently accounted for through the DSM and translates to larger melt pool volumes and variations in melt pool overlap.

In the current work, a conventional snaking scan strategy is utilized by the DSM, where an initial thermal build-up is experienced through

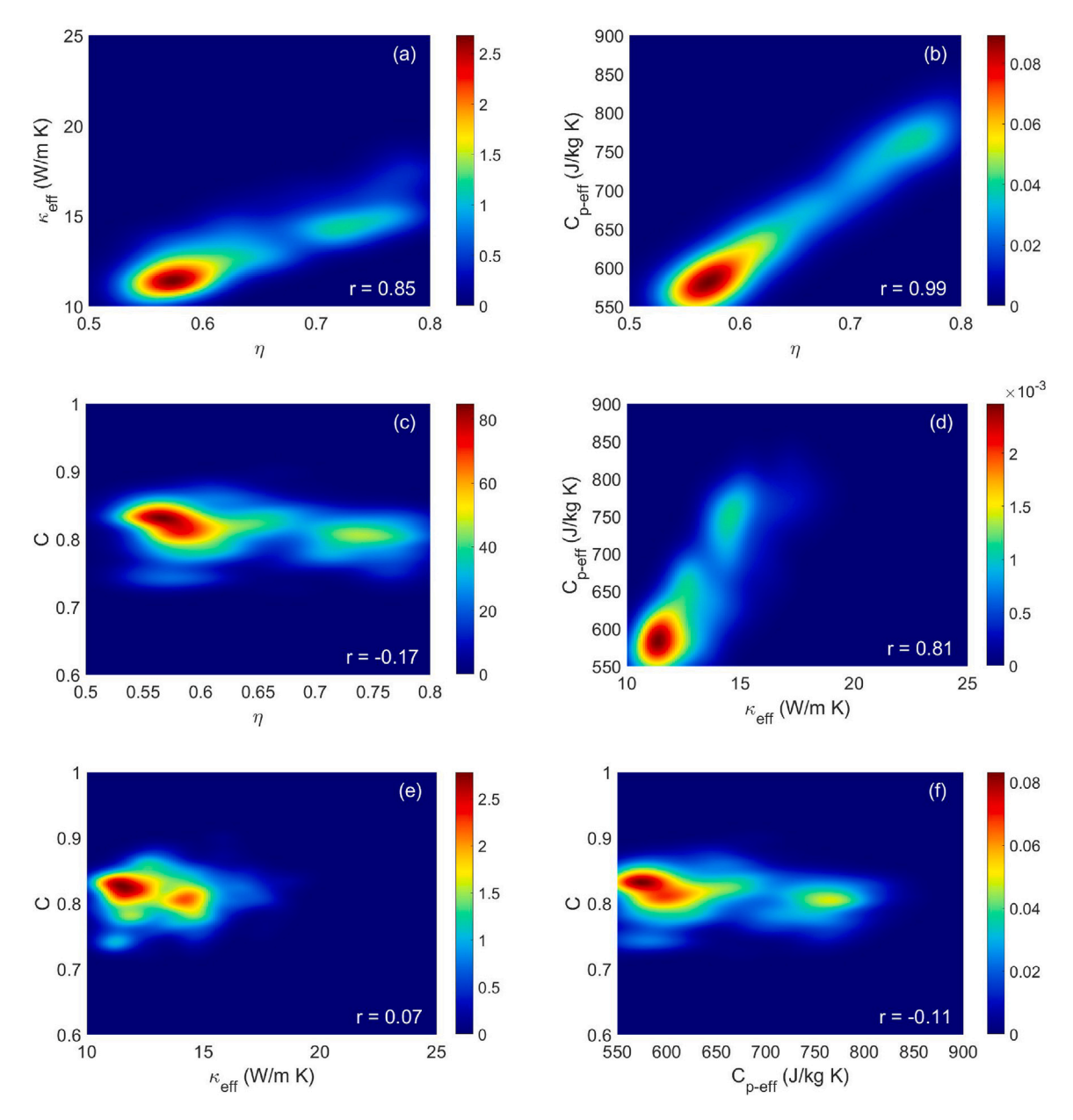


Fig. 5. Bivariate joint posterior PDFs of the DSM parameters obtained after the MCMC calibration against the experimental data for $Ni_{50.3}Ti_{29.7}Hf_{20.0}$ SMA single-track melt pool dimensions.

the first several tracks until an approximately steady-state preheat is experienced by the remaining tracks. These thermal build-up events correspond to an increase in melt pool dimensions for each track until the steady-state intralayer preheating is reached, resulting in approximately equivalent melt pool widths and depths for the remaining tracks. The start of this steady-state region varies between process parameters, but can be leveraged to reduce computational cost by setting a melt pool dimension-based criterion. For this reason, it is assumed that if a point on the current track and a parallel point on the prior track entertain a desired tolerance of $10^{-16}\ \mu m$ in width and depth, then the steady-state region has been reached and all remaining tracks have the same dimensions.

Interlayer preheating refers to the effect of residual heat on the processing of an AM layer resulting from the processing of the prior layer. Again, the influence of interlayer preheating on melt pool dimensions is highly dependent on the AM process parameters and scan strategy. Due to the intrinsic time–temperature process of AM, as a single layer is printed it experiences thermal diffusion and, given enough time,

eventually cools to room temperature. This layer may now act as a substrate and allow the next layer to be printed in conditions similar to the first layer. This results in melt pool dimensions that are constant through each progressive layer. In the case where insufficient time is given between printed layers, the residual heat build-up could result in slightly larger melt pools and variation in melt pool geometry for progressive layers. Therefore, assuming enough time is given to diminish interlayer preheating effects allows the use of a single predicted layer to model all layers of the AM build and reduce the overall computational cost. This directly correlates to the improved efficiency of the model framework for quickly simulating AM components to screen location-specific properties and guide experiments. For this reason, it is assumed that interlayer preheating is negligible.

Similar to preheating effects, the degree of melt pool overlap with adjacent solidified melt pools also varies based on process parameters and scan strategy. In some cases, the degree of melt pool overlap with solidified tracks from the same or previous layer is marginal, resulting in minor interaction and minimal composition evolution.

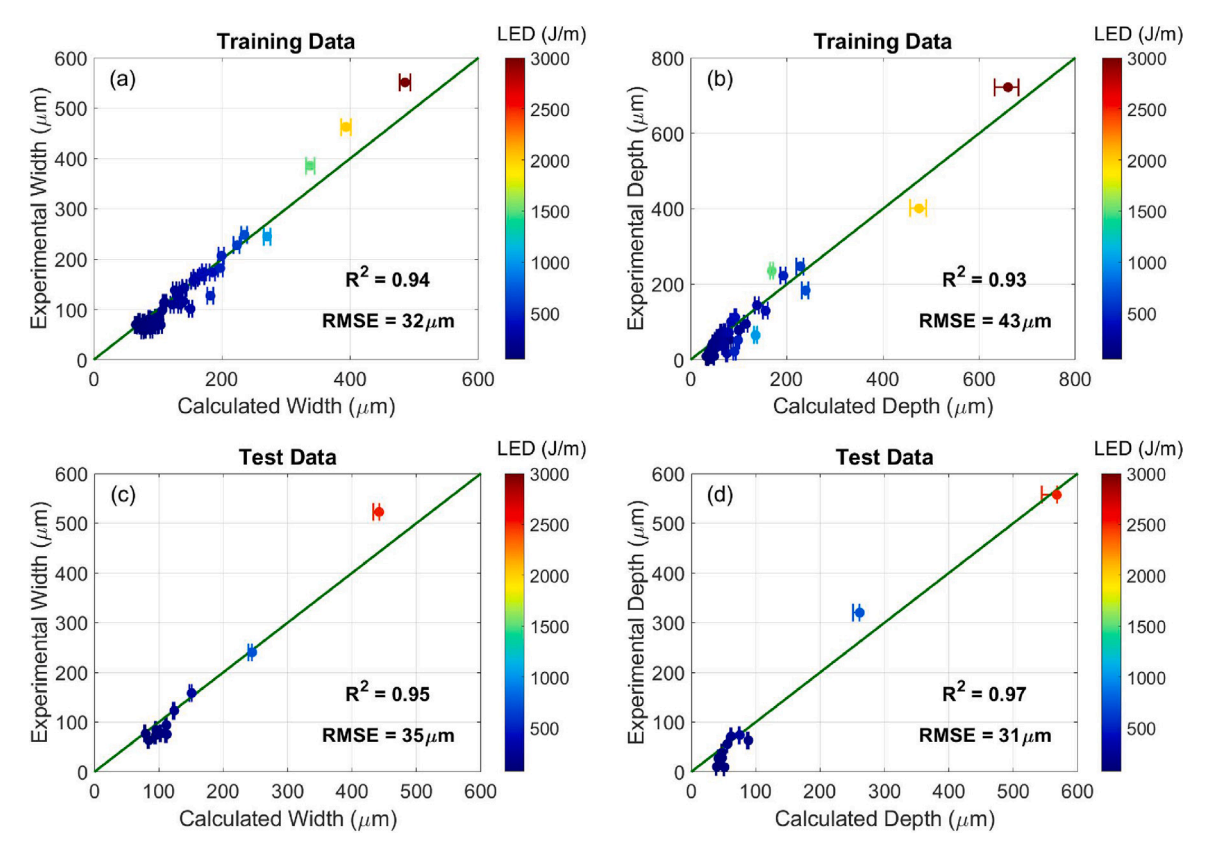


Fig. 6. Calibrated DSM predictions with 95% CIs vs. experimental training and test data for the melt pool width and depth at different given $Ni_{50.3}Ti_{29.7}Hf_{20.0}$ SMA single-track print conditions.

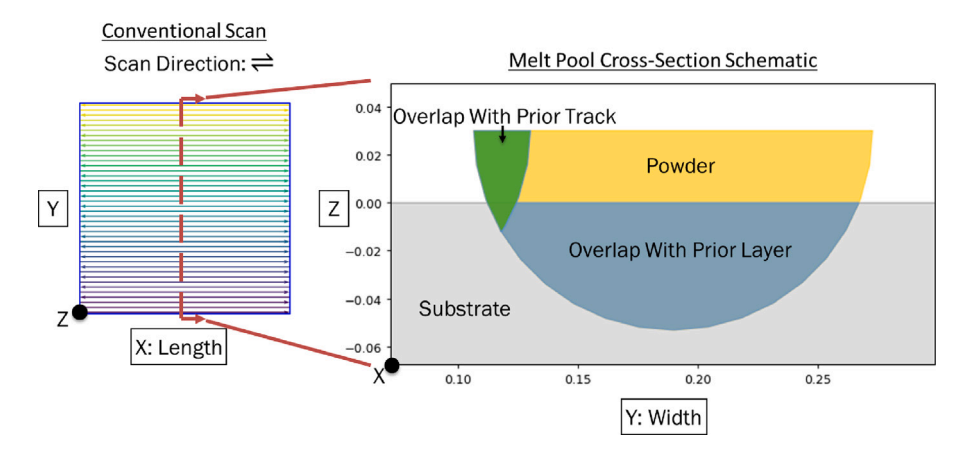


Fig. 7. Conventional snaking scan strategy and melt pool cross-section schematic depicting a sample case for melt pool overlap, where the Z-axis represents the build-direction.

However, the increased computational cost for calculating these small melt pool overlaps remains. For this reason, it is assumed that overlaps comprised of less than 1% of the melt pool cross-sectional area are considered negligible. The implementation and consideration of melt pool overlaps within the model framework are discussed in greater detail in Section 3.1.2.

3.1.2. Melt pool overlap

Melt pool overlap refers to the multiple melting and solidification events occurring on both adjacent tracks and adjacent layers during the AM process, resulting in repeated processing and interaction of melt pool regions. Then by accurately modeling and capturing these melt pool overlaps, the processed composition within each melt pool can be propagated across successive melt pools, resulting in the identification of location-specific composition across the AM part.

The degree of melt pool overlap within an AM build varies based on material properties and process parameters, where process parameters are user-defined. By manipulating process parameters such as hatch spacing, the melt pool overlap and printability of an AM part can be directly controlled, as well as its properties [8]. Scenarios of AM processing with small hatch spacing may produce melt pools which experience overlap with multiple adjacent tracks, while a large enough hatch spacing could result in lack of fusion defects and no overlap. Another aspect to consider with smaller hatch spacing is the corresponding increased volumetric energy density and an increased significance for the evaporation of alloying elements from the melt pool, further influencing location-specific composition and properties. The MLM works in concert with a differential evaporation model discussed in Section 4 to account for the loss of alloying elements due to evaporation. Melt pool overlap is also affected to a varying degree by

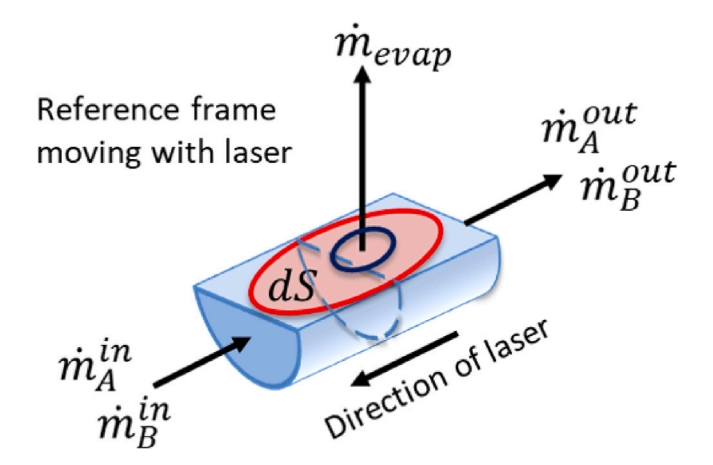


Fig. 8. Mass balance analysis of a melt pool control volume in a reference frame moving with the laser. Republished with permission from [7].

intralayer preheating, which itself is dependent on scan strategy and part geometry. In the current work, the DSM utilizes a conventional snaking pattern along a square geometry with tracks running parallel to the X-axis, as illustrated in Fig. 7. The thermal history within the layer could then be defined by transient regions where thermal events are in greater flux, located near the start and end of each track, and a larger steady-state region where thermal history is constant, located about the center of each track [40]. The melt pool dimensions for a point along a single-track in the steady-state region could then be repeated for remaining points within the steady-state region of the track. Due to the assumption of negligible interlayer preheating and negligible composition effect (across small changes in composition) on melt pool dimensions, this single melt pool can also represent the melt pool dimensions in the proceeding layer. By extension, a slice of resolved melt pool dimensions in the XY-plane, for a single layer, effectively captures and simulates the complete 3D steady-state region of the AM part.

After the AM layers have been simulated, the process of evaluating melt pool overlaps and composition evolution begins with the first melt pool. The melt pool cross-section along the XY-plane is compared with prior melt pool cross-sections along the same plane, as well as the substrate. If no overlap is found, then a lack of fusion defect is likely present and subsequent analysis unnecessary. In the case of multiple overlaps, a precedent is set based on print-time hierarchy. In the case of the first melt pool, the only overlap should be with the substrate. The entirety of the overlap can then be used to determine overlap volume and an average composition calculated based on both powder and substrate volume and composition. This average composition will then be utilized by the differential evaporation model to determine the final solidified melt pool composition after evaporation.

Next, the second melt pool should overlap with the prior melt pool as well as the substrate. Referring to the print-time hierarchy, the overlap with the most recent solidified melt pool should be considered first. From Fig. 7, the referenced overlap could refer to the green region within the melt pool cross-section schematic. This region partially extends into the former substrate region, as it was processed within the first melt pool and corresponds to the first melt pool's calculated composition. The substrate cross-section overlap is then represented by the blue region and substrate composition. Similar to the first melt pool, these overlaps and compositions are then used to determine the second melt pool's average composition. Through this process, the propagation of composition through the first two melt pools has been considered. Similarly, this process can be repeated for remaining melt pools within layer and for proceeding layers, effectively capturing location-specific composition and composition evolution throughout the AM part.

It can be noted that because of constant process parameters and negligible interlayer preheating, a symmetric pattern in melt pool overlap can be drawn from the simulated layers. The number of overlaps will vary based on process parameters, but generally melt pools will only overlap with prior tracks within the same layer and several tracks within the prior layer. Due to consistent depths in the simulated melt pool geometries, melt pools do not extend 2 layers prior and melt pool overlap search criteria can account for this to further reduce computational cost. This is beneficial when an AM part can consist of hundreds of tracks and layers, requiring thousands of melt pools to be accounted for. In the case that variable process parameters modulate within a single build, the search criteria should be re-evaluated to capture appropriate melt pool overlaps and composition evolution.

4. Evaporation induced chemical analysis

4.1. Differential evaporation model

A differential evaporation model (DEM) proposed by [7] is adapted for this work to evaluate melt pool evaporation throughout the AM fabrication process, providing location-specific final composition and transformation temperature properties for the ternary NiTiHf system. The DEM is important in the ICME framework to accurately correlate PSPP relationships by accounting for changes in melt pool composition resulting from the extensive thermal processing and the corresponding evaporation loss of alloying elements experienced by AM components. In this regard, the melt pool post-evaporation predicted composition can be correlated to location-specific properties, such as martensitic start transformation temperature in SMAs. Through the combined DSM-MLM-DEM chain, melt pools and corresponding properties representative of a full-scale AM build can be simulated and used to inform future experiments in the context of AM product design.

4.1.1. Assumptions

The fabrication of an AM part involves the complex interaction of physics between a material and energy source, where accurately capturing the entirety of these interactions is infeasible with current computational methods. In this work, the DEM seeks to leverage the fast-acting DSM and account for missing physics which serve as a loss mechanism within the AM process, important for NiTi-based alloys due to Ni volatility and its evaporation during fabrication. Applying several assumptions, this workflow maintains a reduced computational cost ideal for screening PSPP trends within AM while accounting for material evaporation which prominently affects the composition and properties of AM NiTiHf alloys. These assumptions can then be categorized as the ones related to the prediction of evaporation flux and those corresponding to the calculation of final composition.

When evaluating the thermal processing which occurs during AM fabrication, it is assumed that the flow of molecules during evaporation events abides by The Kinetic Theory of Gases [41]. A formulation for the evaporation flux of a species i, j_i [g/cm²s], is then derived as:

$$j_i = 44.331 \bar{p}_i \left[\frac{M_i}{T_{abs}} \right]^{\frac{1}{2}} \tag{6}$$

where \bar{p}_i [atm] and M_i [g] represent the equilibrium vapor pressure and molecular weight of species i, respectively, and T_{abs} [K] represents the absolute temperature. Additionally, the value 44.331 has the associated units $[\frac{\text{s K}^{1/2} \text{ mol}^{1/2}}{\text{cm g}^{1/2}}]$. The calculation of evaporation flux within the DEM is further explained in Section 4.1.2.

When evaluating the effect of evaporation, it is also assumed that evaporation below the boiling temperature is negligible. This stems from the exponential increase in the vapor pressure and activity, α , of alloying elements with increasing temperature, resulting in the most significant evaporation at the boiling temperature [42]. For this purpose, it is assumed the melt pool surface can be described through the summation of multiple discretized isotherms where the surface

area corresponding to each isotherm domain is defined by a uniform temperature. Additionally, for the case of NiTiHf, Ni experiences the majority of evaporation within the system due to the substantial volatility and large at% of Ni within the NiTiHf system relative to the alloying elements [42]. This change in Ni content should result in an increase in the at% of Hf and Ti. However, also noting insufficient experimental data for M_s across a range of Hf at% in NiTiHf $_X$ and a reduced M_s -Hf sensitivity in the (20 ± 1) at% range relative to M_s -Ni in the 49.8 at.% - 50.8 at.% range [6], Hf at% is assumed to be a constant 20 at.% for model predictions in this work. This assumption is further expanded upon in Section 4.1.3. As a result, an increase in Ti at% accounts for the corresponding loss in Ni content. Furthermore, through these assumptions, a reduction in the number of calculations and the total computational cost is achieved for the sake of the efficient establishment of PSPP relationships towards AM product design.

After quantifying evaporation loss from the melt pool, the associated change in composition of the melt pool must also be accounted for. For this purpose, it is assumed that the melt pool can be defined as a mass balance problem of a control volume. This is accompanied by a formulation for the mass flow in, \dot{m}^{in} , the mass flow out, \dot{m}^{out} , and the mass loss due to evaporation from the system, \dot{m}^{evap} :

$$\dot{m}^{out} = \dot{m}^{in} - \dot{m}^{evap} \tag{7}$$

The mass balance and composition change is discussed further in Section 4.1.2. However, to make these calculations tractable, a secondary assumption is made. Here it is assumed that the flow of material within the melt pool allows for the complete mixing of the contained elements. Through this assumption, an average composition can be determined for a given melt pool and utilized within the model framework for the calculation of location-specific final composition as well as composition evolution throughout the component.

4.1.2. Composition change

In order to calculate the composition change within a melt pool, the mass balance described by Eq. (7) must be resolved. Illustrated by Fig. 8, this control volume analysis of the melt pool is in a reference frame moving with the laser [7].

Here, both the mass flow into and out of the control volume may be deconstructed as a function of density, ρ [kg/m³], and flow velocity, ν [m/s], over the cross-sectional area, A_{x-s} [m²], of the control volume:

$$\dot{m} = \int (\rho \omega v) dA_{x-s} \tag{8}$$

Solving for \dot{m}^{in} and \dot{m}^{out} , while accounting for the weight fraction, ω , of the alloying species i, yields:

$$\dot{m}_i^{in} = \rho^{in} \omega_i^{in} v A_{x-s}^{in} \tag{9}$$

$$\dot{m}_i^{out} = \rho^{out} \omega_i^{out} v A_{r-s}^{out} \tag{10}$$

The mass flow out of the melt pool due to evaporation for each alloying species i, m_i^{evap} , can then be similarly deconstructed as:

$$\dot{m}_{i}^{evap} = \sum_{iso=1}^{n} j_{i} \left(\chi_{A}, \chi_{B}, \dots, T_{iso} \right) S_{iso}$$
(11)

where the evaporation rate for a species i, j_i , is dependent on both the composition of the alloying elements and an isotherm temperature, (χ_A, χ_B, \ldots) and T_{iso} , respectively. This evaporation rate is multiplied with the corresponding surface area of the isotherm, S_{iso} . The meltpool surface can be discretized into multiple temperature isotherm bins, n, and summed to determine the total mass loss of the alloying species due to evaporation. However, due to the simplifying assumption of negligible evaporation below the boiling temperature, this equation is reduced to:

$$\dot{m}_{i}^{evap} = j_{i} \left(\chi_{A}, \chi_{B}, \dots, T_{boil} \right) A_{boil}$$
(12)

Table 3
Antoine coefficients for Ni Ti and Hf

rantomic cocinicionio for fin, fin, and fini							
Element	\mathbf{A}_A	B_A [°C]	C_A [°C]				
Ni	8.75	17882.38	134.99				
Ti	8.90	20948.99	190.76				
Hf	9.06	30232.91	285.82				

The reader is referred to Ranaiefar et al. [7] for additional details on the mass balance in a control volume derivation. However, from Eqs. (7)–(12), a first-order solution to the problem, describing the mass flow due to each alloying species i through the melt pool, can be rewritten as:

$$\dot{m}_{i}^{out} = \rho^{in} \omega_{i}^{in} v A_{x-s}^{in} - j_{i} \left(\chi_{A}, \chi_{B}, \dots, T_{boil} \right) A_{boil}$$
(13)

As part of this solution, further decomposition of variable components for evaporation flux, Eq. (6), is required. The equilibrium vapor pressure for an alloying species i can be calculated through the product of standard vapor pressure and activity for the species i, p_i° [atm] and α_i , respectively, as [43]:

$$\bar{p}_i = p_i^{\circ} \alpha_i \tag{14}$$

It should be noted that activity values were generated through the Thermocalc 2020b TCHEA4 database and are not easily measured. For this reason, Ni activity, corresponding to the most volatile and prominent constituent of the NiTiHf system is subject to calibration in Section 4.4. Furthermore, the standard vapor pressure of a species i is determined through an empirical expression, derived from the Clausius–Clapeyron relation, dependent on temperature, T [°C], and a set of species dependent Antoine coefficients, $A_{A,i}$, $B_{A,i}$ [°C], and $C_{A,i}$ [°C]:

$$p_i^{\circ} = 10^{\left(A_{A,i} - \frac{B_{A,i}}{C_{A,i} + T}\right)} 760^{-1}$$
 (15)

Here, the coefficient $\frac{1}{760}$ has associated units $\left[\frac{alm}{mmHg}\right]$. With Antoine coefficients corresponding to each alloying element of the NiTiHf system [42], defined in Table 3, a solution to mass loss and composition change in a melt pool due to evaporation can be determined. Based on the low vapor pressure of Hf within the system, it should be noted that the evaporation flux of Hf is set to zero.

4.1.3. Nickel-martensitic transformation temperature (m_s) relationship

The binary NiTi SMA has been widely studied in literature, where current challenges include a lack of technologically advanced tools, with sufficient precision, for the chemical analysis and exact measurement of Ni content in these alloys [3,44,45]. Due to the addition of ternary Hf, measurement of Ni-content within the NiTiHf system is made further difficult [6,46,47]. Additionally, mapping the M_s -Ni relationship becomes more difficult in this case, as M_s is highly sensitive to both Ni and Hf content. However, as mentioned in Section 4.1.1, these SMAs can be treated the same as binary NiTi SMAs since it is assumed that only their Ni content changes during the fabrication process, due to the significantly greater volatility of this element. Due to Hf's negligible evaporation and noting insufficient experimental data for M_s at other NiTiHf compositions, Hf content remains at a constant 20 at.% for model predictions in this work, where any associated error is covered by the estimation of the overall model uncertainty. Fig. 9 illustrates the M_s -Ni relationship for the NiTiHf system with a constant Hf content, χ_{Hf} , of 20 at.%.

It is shown that at Ni-rich content, a decrease in just 0.2 Ni at% can result in a ΔM_s of 100 °C. This strong negative trend of increasing M_s with decreasing Ni content eventually weakens as M_s reaches an approximate peak of 306 °C at 49.8 Ni at%. Overall, this trend lends to reinforcing the extreme sensitivity of M_s with Ni content along with the importance and potential for utilizing this relationship to

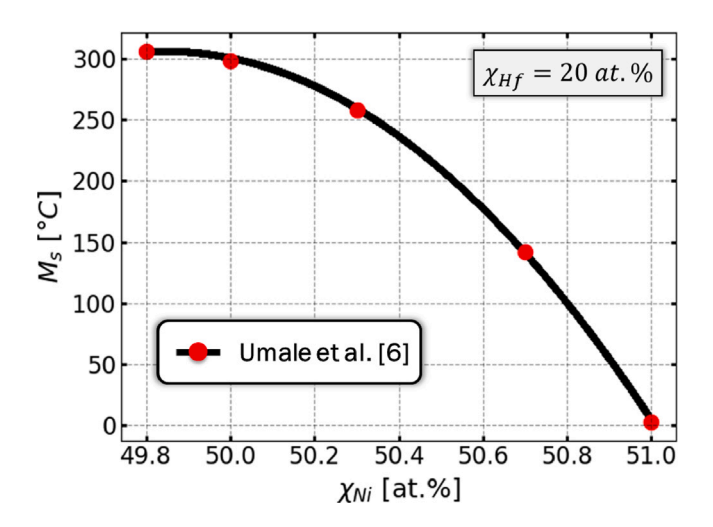


Fig. 9. Relationship between Ni content, χ_{Ni} [at%], and martensitic start transformation temperature, M_s [°C].

tailor location-specific properties of NiTiHf SMA components manufactured by LPBF. From DSC measured Ni $_x$ Ti $_Y$ Hf $_{20}$ data [6], an empirical relation describing the M_s -Ni relationship can be developed:

$$M_s(\chi_{Ni}) = -225.834\chi_{Ni}^2 + 22513.431\chi_{Ni} - 560785.997$$
 (16)

This formulation is then used in the current study to link predicted location-specific Ni content to the martensite start transformation temperature property.

It should also be noted that although the as-received NiTiHf ingots used in this work had a reported Ni content of 50.3 at.%, discussed in Section 2.2, the solutionized powder M_s value was measured as 101.9 °C through differential scanning calorimeter characterization. Based on Fig. 9 and Eq. (16), this M_s value is best characterized by a Ni content of 50.8 at.%. Therefore, for the current work, model predictions for the NiTiHf system will utilize Ni $_{50.8}$ Ti $_{29.2}$ Hf $_{20}$ as the initial powder composition.

4.2. Experimental procedure

The 26 cuboid NiTiHf samples with size of 10 mm \times 10 mm \times 5 mm (building direction) were fabricated on NiTi substrates using DMP ProX 200 LPBF system under argon atmosphere. The oxygen level was kept below 100 ppm during the fabrication process to mitigate potential oxidation and associated performance degradation. Cell scanning strategy with cell size of 3 mm, overlap of 0.3 mm, and rotation of 67° between sequential layers was applied to reduce residual stress build-up. Within each cell, the normal back-and-forth laser paths were applied orthogonal to cell edges.

After printing, the cuboid NiTiHf samples were wire-EDM cut from the substrates for further characterization. A TA Instruments Q2000 differential scanning calorimeter (DSC) was used to measure the transformation temperatures of the fabricated samples. For each cuboid sample, the DSC specimen with 1 mm thickness and 3 mm diameter was cut from the middle of the cuboid sample and solution heat treated at 900 °C for 1 h followed by water quenching before DSC characterization. Two thermal cycles from 25 to 400 °C were performed at the heating/cooling rate of 10 °C/min. The transformation temperatures were then obtained from the plots of the second cycles using the tangent method according to ASTM F2004-17. Table 4 contains the solution heat-treated (SHT) M_s data corresponding to laser power, P, laser speed, v, hatch spacing, h_s , linear energy density (LED), and volumetric energy density (VED) of 26 experiments with a constant layer thickness, L_t , of 41 µm. Furthermore, the data is identical to that of Zhang et al. [8], which can be referenced for additional information on the experimental details.

Table 4 Process parameters and transformation temperatures after solution heat treatment of 26 LPBF fabricated $Ni_{50.3}Ti_{29.7}Hf_{20}$ cuboid specimens.

P [W]	υ [mm/s]	h _s [μm]	LED [J/m]	VED [J/mm ³]	SHT M _s [°C]
80	330	40	242.4	147.8	305.8
100	455	40	219.8	134.0	297.8
100	600	75	166.7	54.2	201.8
100	600	40	166.7	101.6	215.2
100	600	30	166.7	135.5	300.9
100	600	26	166.7	156.3	325.5
100	600	20	166.7	203.3	309.9
100	800	87	125.0	35.0	191.2
100	800	60	125.0	50.8	198.0
100	800	40	125.0	76.2	256.2
100	800	30	125.0	101.6	262.7
100	800	25	125.0	122.0	316.1
100	800	20	125.0	152.4	305.3
100	800	15	125.0	203.3	308.9
100	800	12	125.0	254.1	313.6
120	830	35	144.6	100.8	212.4
120	830	25	144.6	141.1	274.6
120	830	18	144.6	196.0	304.9
120	1080	77	111.1	35.2	187.7
120	1080	50	111.1	54.2	194.4
120	1080	36	111.1	75.3	236.8
120	1080	27	111.1	100.4	286.0
120	1080	20	111.1	135.5	313.7
120	1080	13	111.1	208.5	314.9
120	1080	10	111.1	271.0	329.6
140	1080	25	129.7	126.5	251.1

4.3. Calibration approach

Although the DSM can directly utilize MCMC sampling for Bayesian calibration due its low computational cost, the combined DSM-MLM-DEM chain has an added computational expense where the utilization of a surrogate model could reduce the complexity of the coupled models and hence offset the overall cost to run tens of thousands of simulations across the full model framework. Such an advantage is especially important for the implementation of MCMC based uncertainty quantification and the Bayesian calibration method. In this section, a computationally cheap surrogate for the DSM-MLM-DEM chain is developed. However, the prediction performance of the surrogate model is influenced by various uncertainties. One major uncertainty source is from the simulation data used for surrogate training, which stems from model assumptions and simplifications in the DSM, MLM and DEM. Another key contribution to uncertainty is from the assumption that the surrogate is a Gaussian process model. Additionally, the unknown Ni activity parameter also brings uncertainty into the system. To quantify the prediction error of the surrogate model, the Ni activity parameter is sampled 10,000 times from Uniform (0.15, 0.4). We predict M_s at 26 sets of process parameters, each with 95% confidence bands. As shown in Fig. 10, the surrogate model has great uncertainty in prediction and probabilistic calibration is required.

To further calibrate the Ni activity parameter and correct the bias of the surrogate model, the statistical model proposed by [23], deemed the Kennedy and O'Hagan (KOH) framework, is applied:

$$z_{i} = S \eta_{s} \left(\mathbf{x}_{i}, \boldsymbol{\theta} \right) + \delta(\mathbf{x}_{i}) + e_{i} \tag{17}$$

where S is a scaling parameter, \mathbf{x} is control inputs, $\boldsymbol{\theta}$ is calibration parameters, $\eta_s(\cdot,\cdot)$ is the surrogate model output, $\delta(\cdot)$ is the model discrepancy term, z_i is the ith experimental observation and e_i is the ith observation error. $\eta_s(\cdot,\cdot)$, $\delta(\cdot)$, and z_i are assumed to be mutually independent.

Specifically, e_i is an independently distributed Gaussian noise with zero mean and a constant variance σ_{ϵ}^2 , i.e., $e_i \sim N(0, \sigma_{\epsilon}^2)$. $\eta_s(\cdot, \cdot)$ and $\delta(\cdot)$ follow Gaussian process distributions with different mean function and covariance function, i.e., $\eta_s(\cdot, \cdot) \sim \text{GP}(m_1(\cdot, \cdot), c_1(\cdot, \cdot))$ and $\delta(\cdot) \sim \text{GP}(m_1(\cdot, \cdot), c_1(\cdot, \cdot))$

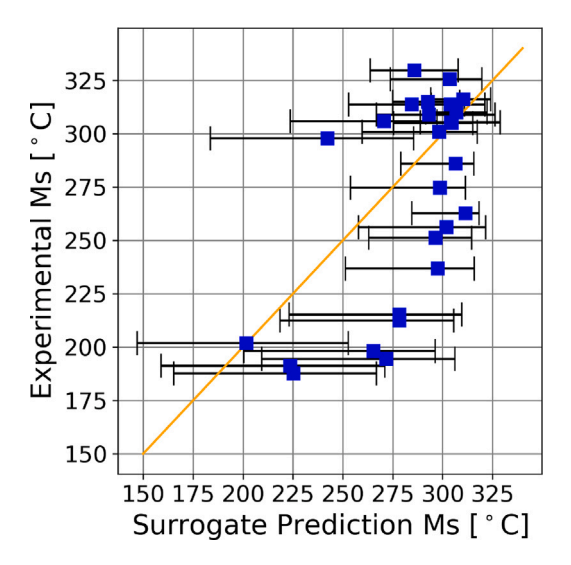


Fig. 10. Prediction performance of the DSM-MLM-DEM surrogate with 95% confidence bands.

GP($m_2(\cdot), c_2(\cdot, \cdot)$). We adopt a linear form for the mean function, therefore $m_1(\mathbf{x}, \mathbf{t}_{\theta}) = \mathbf{h}_1(\mathbf{x}, \mathbf{t}_{\theta})^{\mathsf{T}} \boldsymbol{\beta}_1$ and $m_2(\mathbf{x}) = \mathbf{h}_2(\mathbf{x})^{\mathsf{T}} \boldsymbol{\beta}_2$. It is well known that selecting a well-fit covariance function (also called kernel) and choosing proper kernel hyperparameters (denoted as $\boldsymbol{\psi}$) are nontrivial jobs in GP modeling. The goal of calibration is to use simulation data \mathbf{y}^{T} and experimental observations \mathbf{z}^{T} to estimate linear estimates $\boldsymbol{\beta} = (\boldsymbol{\beta}_1^{\mathsf{T}}, \boldsymbol{\beta}_2^{\mathsf{T}})^{\mathsf{T}}$, system hyperparameters $\boldsymbol{\phi} = \{S, \boldsymbol{\psi}, \sigma_{\epsilon}^2\}$, and calibration parameters $\boldsymbol{\theta}$. These parameters should be independent of each other, so the prior distributions is:

$$p(\boldsymbol{\beta}, \boldsymbol{\theta}, \boldsymbol{\phi}) = p(\boldsymbol{\beta})p(\boldsymbol{\theta})p(\boldsymbol{\phi}) \tag{18}$$

For data $\mathbf{d} = (\mathbf{y}^{\mathsf{T}}, \mathbf{z}^{\mathsf{T}})^{\mathsf{T}}$, its likelihood function is $p(\mathbf{d}|\boldsymbol{\theta}, \boldsymbol{\phi}, \boldsymbol{\beta})$. Using the Bayes' rule, we are able to obtain the posterior distribution:

$$p(\boldsymbol{\beta}, \boldsymbol{\theta}, \boldsymbol{\phi} | \mathbf{d}) \propto p(\mathbf{d} | \boldsymbol{\beta}, \boldsymbol{\theta}, \boldsymbol{\phi}) p(\boldsymbol{\beta}) p(\boldsymbol{\theta}) p(\boldsymbol{\phi})$$
(19)

In order to efficiently conduct calibration, we use the two-step strategy by [23] to estimate hyperparameters ϕ . The first step is to tune the surrogate model using simulation data, namely to estimate the hyperparameters ψ_1 of $c_1(\cdot,\cdot)$; next, fix ψ_1 and use data \mathbf{d} to estimate $\{S,\psi_2,\sigma_{\epsilon}^2\}$. Based on the distribution of MCMC samples, we take the posterior estimates in the form of the maximum a posterior probability (MAP) estimates or posterior means. Conditional on the estimated parameters, the calibrated model $\mathbf{z}(\mathbf{x}_0)$ with input \mathbf{x}_0 is a Gaussian process, its mean and covariance functions are expressed as follows:

$$\mathbb{E}[\mathbf{z}(\mathbf{x}_0)|\mathbf{d},\theta,\phi] = \mathbf{h}(\mathbf{x}_0,\theta)^{\mathsf{T}}\hat{\boldsymbol{\beta}}(\theta) + \mathbf{t}(\mathbf{x}_0,\theta)^{\mathsf{T}}\boldsymbol{\Sigma}(\theta)^{-1}(\mathbf{d} - \mathbf{H}(\theta)\hat{\boldsymbol{\beta}}(\theta)) \tag{20}$$

$$\begin{split} \mathbb{COV}[\mathbf{z}(\mathbf{x}_0)|\mathbf{d},\boldsymbol{\theta},\boldsymbol{\phi}] &= S^2 \ c_1((\mathbf{x}_0,\boldsymbol{\theta}),(\mathbf{x}_0,\boldsymbol{\theta})) + c_2(\mathbf{x}_0,\mathbf{x}_0) - \mathbf{t}(\mathbf{x}_0,\boldsymbol{\theta})^\intercal \boldsymbol{\Sigma}(\boldsymbol{\theta})^{-1} \mathbf{t}(\mathbf{x}_0,\boldsymbol{\theta}) \ & + (\mathbf{h}(\mathbf{x}_0,\boldsymbol{\theta}) - \mathbf{H}(\boldsymbol{\theta})^\intercal \boldsymbol{\Sigma}(\boldsymbol{\theta})^{-1} \mathbf{t}(\mathbf{x}_0,\boldsymbol{\theta}))^\intercal \mathbf{W}(\boldsymbol{\theta})(\mathbf{h}(\mathbf{x}_0,\boldsymbol{\theta}) \\ & - \mathbf{H}(\boldsymbol{\theta})^\intercal \boldsymbol{\Sigma}(\boldsymbol{\theta})^{-1} \mathbf{t}(\mathbf{x}_0,\boldsymbol{\theta})) \end{split}$$

where

$$\begin{split} \mathbf{h}(\mathbf{x}_0,\theta) &= [S \ \mathbf{h}_1(\mathbf{x}_0,\theta) \quad \mathbf{h}_2(\mathbf{x}_0)]^{\mathsf{T}} \\ \mathbf{t}(\mathbf{x}_0,\theta) &= [S \ c_1((\mathbf{x}_0,\theta),D_1) \quad S^2 \ c_1((\mathbf{x}_0,\theta),D_2(\theta)) + c_2(\mathbf{x}_0,D_2)]^{\mathsf{T}} \\ \mathbf{H}(\theta) &= \begin{bmatrix} \mathbf{H}_1(D_1) & \mathbf{0} \\ S \ \mathbf{H}_1(D_2(\theta)) & \mathbf{H}_2(D_2) \end{bmatrix} \\ \mathbf{\Sigma} &= \begin{bmatrix} c_1(D_1,D_1) & S \ c_1(D_1,D_2(\theta)) \\ S \ c_1(D_2(\theta),D_1) & \sigma_{\varepsilon}^2 \mathbf{I} + S^2 \ c_1(D_2(\theta),D_2(\theta)) + c_2(D_2,D_2) \end{bmatrix} \\ \mathbf{W} &= (\mathbf{H}(\theta)^{\mathsf{T}} \mathbf{\Sigma}(\theta)^{-1} \mathbf{H}(\theta))^{-1} \end{split}$$

 D_1 is the inputs of simulation data \mathbf{y}^{\intercal} , containing control inputs and calibration inputs; D_2 is the control inputs of experimental measurements \mathbf{z}^{\intercal} ; $D_2(\theta)$ combines D_2 with the estimates of calibration parameters. $\mathbf{H}_i(D_j)$ is the matrix form of \mathbf{h}_i^{\intercal} on D_j , for example, the ith row of $\mathbf{H}_2(D_2)$ takes the form of $\mathbf{h}_2(\mathbf{x}_i)^{\intercal}$.

4.4. Calibration results

The proposed differential evaporation model takes power P, velocity, v, and hatch spacing, h_s , as control inputs, i.e., $\mathbf{x} = \{P, v, h_s\}$ and Ni activity as the calibration parameter, i.e., $\theta = \{\alpha_{Ni}\}$. The prediction of the model is the martensite start transformation temperature, denoted as M_s . For surrogate model development, 556 data points were generated uniformly over the parameter space $\mathcal{X} \times \Theta$, bounded by experiment conditions, using Latin Hypercube Sampling.

Before modeling, the mean and covariance functions of the GP models should be specified. We take $\mathbf{h}_1(\mathbf{x},\mathbf{t}_\theta)=\mathbf{h}_2(\mathbf{x})=(1)$; for surrogate model we adopt the Matérn kernel (ν =3/2), with hyperparameters $\psi_1=\{\sigma_s^2,\ell_s\}$; for discrepancy model we define its covariance function with hyperparameters $\psi_2=\{\sigma_{\delta_s}^2,\sigma_{\delta_s}^2,\ell_1,\ell_2,\ell_3\}$:

$$c_2(\mathbf{x}, \mathbf{x}') = \sigma_{\delta_1}^2 \prod_{i=1}^3 \exp\left(-\frac{(\mathbf{x}_i - \mathbf{x}_i')^2}{2\ell_i^2}\right) + \sigma_{\delta_2}^2 \mathbf{x} \mathbf{x}'^{\mathsf{T}} + \sigma_{\delta_3}^2$$
(22)

As explained in Section 4.3, the first step is training the surrogate model. With 90% 10-fold cross validation accuracy, a zero-mean (namely $\beta_1 = 0$), Matérn ($\nu = 3/2$) kernel GP model was selected and trained on 556 simulation data using the *GaussianProcessRegressor* function through the Python scikit-learn package by [48], outputting hyperparameters $\psi_1 = \{0.655, 0.328\}$.

For remaining hyperparameters $\{S, \psi_2, \sigma_e^2\}$, coefficient β_2 and calibration parameter θ , MCMC is used for generating samples. Since there is little knowledge of unknown calibration parameter, except for its domain, a weak uniform prior is commonly used for θ . As for other hyperparameters $\in \mathcal{R}^+$, informative inverse-gamma or log-normal priors are assigned. The prior distributions are set as follows:

$$\theta \sim \text{Uniform}(0.15, 0.4)$$

$$\sigma_{\delta_1}^2, \ \sigma_{\delta_3}^2 \sim \text{Inverse} - \text{Gamma}(\alpha = 2, \beta = 1)$$

$$\sigma_{\delta_2}^2, \ \sigma_{\epsilon}^2, \ \beta_2 \sim \text{Inverse} - \text{Gamma}(\alpha = 2, \beta = 0.1)$$

$$S, \ \ell_i \sim \text{Log} - \text{Normal}(\mu = 0, \sigma^2 = 1/4), \ i = 1, 2, 3$$

From the 26 cuboid experiment parameter sets, 20 were randomly selected as training data and the remaining 6 points were used as test data. MCMC was run in Python using PyMC3 [49]. Two chains of samples, with the sample size of 30,000 and tuning size of 10,000, were generated. We took the posterior mean of α_{Ni} as the posterior estimate, i.e., $\theta^* = 0.275$. For the hyperparameter $\phi = \{S, \{\sigma_{\delta_1}^2, \sigma_{\delta_2}^2, \sigma_{\delta_3}^2, \ell_1, \ell_2, \ell_3\}, \sigma_{\epsilon}^2\}$, $\phi_{MAP}^* = \{0.560, \{0.585, 0.030, 0.455, 0.937, 0.792, 0.452\}, 0.069\}$ and coefficients MAP estimates are $\hat{\beta} = [0, 0.047]^{\text{T}}$.

According to Eq. (20), M_s for the test points can now be predicted. Table 5 contains performance metrics of model predictions against experimental measurements, for the 6 test data points, in terms of the root mean squared error (RMSE) and mean absolute percentage error (MAPE) for both the surrogate $(\alpha_{Ni} = \theta^*)$ and calibrated model. Upon evaluation, the calibrated model achieved an RMSE and MAPE value of 11.8 °C and 3.1%, respectively, in contrast to the surrogate model's RMSE of 17.0 °C and MAPE of 5.9%. These results make evident the effective improvement in the predictive power of the model resulting from Bayesian calibration.

Furthermore, through uncertainty quantification of the calibrated model parameter, Ni activity, increased comprehension of the model framework's utility for the purpose of robust design can be ascertained. Fig. 11 illustrates the propagated uncertainty through the multi-model framework for each of the 26 LPBF NiTiHf parameter sets, stemming from MCMC samples generated through the calibration of the DEM. In

Table 5 Performance metrics for the surrogate ($\alpha_{Ni} = \theta^*$) prediction and calibrated prediction on the 6 test data points.

Model	RMSE [°C]	MAPE [%]
Surrogate	17.0	5.9
Calibrated	11.8	3.1

RMSE — root mean square error; MAPE - mean absolute percentage error.

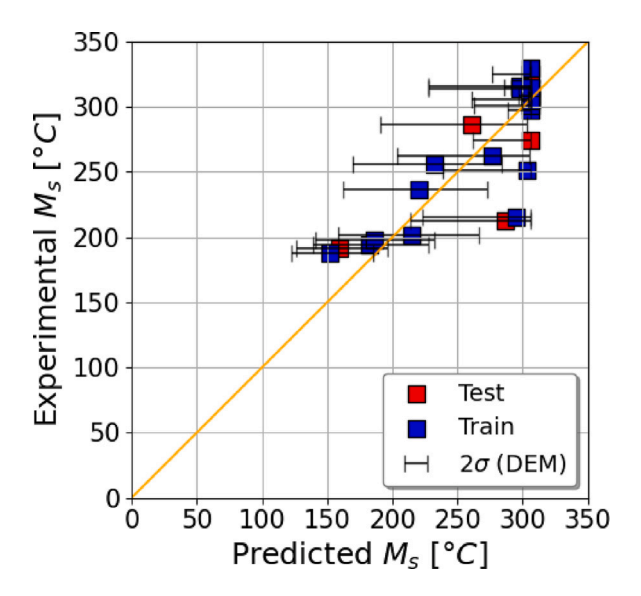


Fig. 11. Uncertainty propagation with 95% CIs for model predictions of M_s compared with empirical values for LPBF Ni_{50.3}Ti_{29.7}Hf₂₀ samples. Here, uncertainty propagation is from the DEM only.

this case, the last 500 samples for the Ni activity parameter selected from each of the two MCMC sample chains (generated from two different initial parameter values) are combined and used as model input, after which the top and bottom 2.5% output values, i.e., M_s , are removed for each experimental condition to provide a 95% CI. Through this uncertainty quantification, experimental measurements are shown to fall within the 95% CIs of model predictions, with the exception of three cases. In Section 5, the total model uncertainty and 95% CIs are determined and compared with experiments to provide a complete and more robust measure of the model framework's utility for AM design.

5. Model validation and discussion

Through the calibrated ICME framework, M_s properties were predicted and validated with the 26 LPBF NiTiHf cuboids discussed in Section 4.2 Table 4. The model framework input parameters and thermophysical properties are listed in Table 6.

5.1. Probabilistic model prediction in the presence of experimental uncertainties

In addition to model uncertainties due to assumptions and missing physics, expressed in Section 2 through Section 4, there are several sources of experimental uncertainties contributing to variation in reported process–structure–property relationships. These experimental uncertainties stem from the initial powder composition measurement, melt pool dimension measurements due to melt pool non-uniformity across single-track prints, and transformation temperature measurement of NiTiHf through DSC. It should also be reiterated that although calibration, conducted in Section 2.3 and Section 4.3, does not fix experimental measurement uncertainties and uncertainties pertaining

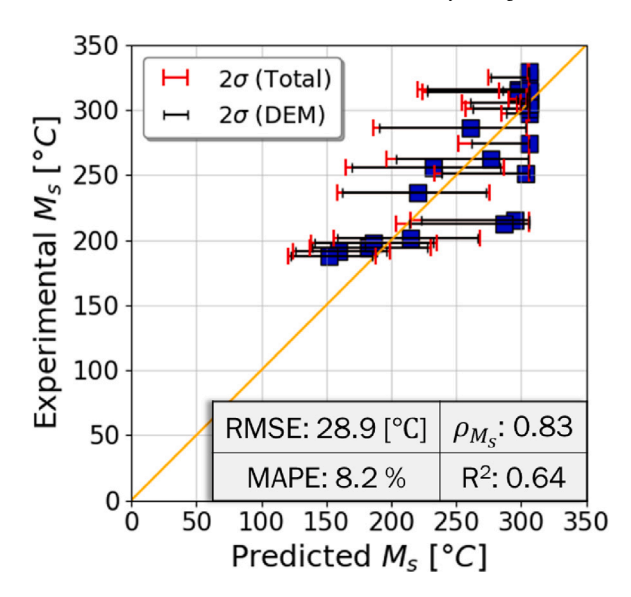


Fig. 12. Model predictions of M_s with their 95% CIs compared with empirical values for LPBF Ni_{50.3}Ti_{29.7}Hf₂₀ samples, resulting from DEM uncertainty propagation only and uncertainty propagation for all components of the ICME framework.

to missing physics in the applied models, if measured M_s values are captured within the uncertainty bounds of predictions, this is sufficient proof for the utility of the model chain towards material and process design.

Fig. 12 provides a comparison of model predictions for M_s and DSC measurements from experiments. The root mean square error (RMSE) and mean absolute percentage error (MAPE) for the 26 samples is 28.9 °C and 8.2%, respectively, representing a good measure of predictive accuracy for the model when compared with experiments. Furthermore, the Pearson correlation, $\rho_{M_{\rm c}}$, of 0.83 indicates a strong positive linear correlation between predicted and measured M_s . The coefficient of determination, R^2 , of 0.64 demonstrates a moderate ability for predicting M_s , which, coupled with uncertainty quantification, provides sufficient utility for design. The strength of these predictions is further reinforced when considering the uncertainty of standard composition measurement techniques such as wavelength dispersive spectroscopy (WDS) and inductively coupled plasma atomic emission spectroscopy (ICP-AES), \pm 0.5 at.%. Additionally, for the measurement of major constituents, ICP-AES uncertainty has been reported to be as large as $\pm 2\%$ of the absolute value [50]. Converting Ni content measured through these techniques to M_s could then result in an uncertainty of ±75 °C. This demonstrates the model framework's capability to accurately and efficiently predict M_s property values from processing parameters, performing well within the range of uncertainty for composition measurement techniques.

Equally important in understanding the utility of the model framework for the purpose of robust design, uncertainty quantification through the uncertainty propagation of calibrated model parameters has been conducted. Fig. 13 illustrates the propagated uncertainty through the model framework for each of the 26 LPBF NiTiHf conditions, stemming from MCMC samples generated through the calibration of both the DSM and the DEM. In this case, the last 1000 MCMC samples from the DSM calibration and the same 1000 samples from the prior DEM uncertainty propagation, Section 4.4, are combined and used as model input. The top and bottom 2.5% output values are then removed to provide 95% CIs for model predictions based on the uncertainty propagation across the entire model framework.

It should be noted that the model framework was run on Texas A&M University's High Performance Computing Research platform GRACE. Multiple parameter sets were run in parallel, utilizing a portion of the

Table 6
Model input parameters and thermophysical properties for the 26 LPBF NiTiHf experiments.

				•	κ [W/m K]	C _p [J/kg K]	С	σ [μm]	ρ [kg/m ³]	T ₀ [°C]
80-140	330-1080	10-87	41	0.64	13.2	652.5	0.81	20	8893	25

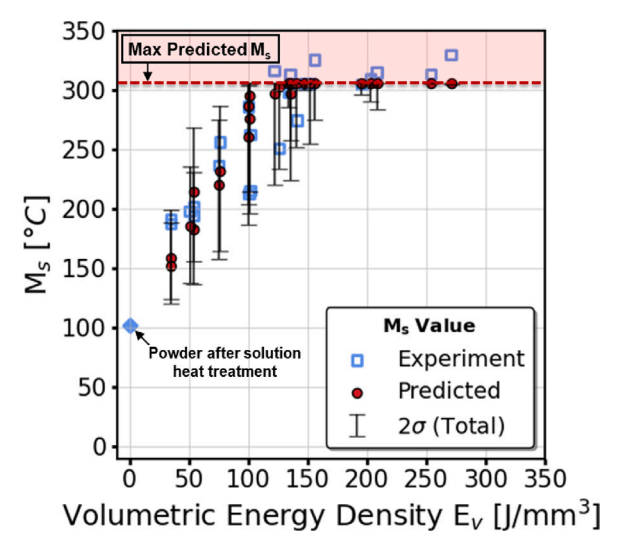


Fig. 13. Model predictions of M_s with their 95% CIs in terms of VED for LPBF $\mathrm{Ni}_{50.3}\mathrm{Ti}_{29.7}\mathrm{Hf}_{20}$ samples, resulting from uncertainty propagation for all components of the ICME framework.

800 48-core computer nodes with 384 GB RAM (dual socket server with two Intel 6248R 3.0 GHz 24-core processors). With these resources, the DSM can predict the width and depth of a melt pool in several seconds. The melt pool length calculation extends this computation to several minutes. The computational time of evaluating melt pool overlaps through the MLM and subsequent chemistry propagation through the DEM across multiple tracks and layers can vary greatly based on process parameters. This can range from 1 to 4 h for several thousand melt pool evaluations and results in location-specific composition predictions.

When comparing uncertainty from the DEM alone to the complete framework uncertainty, an increase in the range of the 95% CI is observed. This is expected due to the consideration of increased uncertainty stemming from the DSM. It should be noted that the peak M_s set by Eq. (16) results in uncertainty bounds which do not capture M_s values exceeding 306 °C, although the model predictions still follow experimental trends. This is observed for higher VED cases, where increased Ni evaporation and M_s values are expected, and can be resolved through additional experiments to refine the empirical Ni- M_s relationship. Furthermore, with experimental measurements falling within the 95% confidence interval of model predictions, the calibrated ICME framework demonstrates its utility and potential to guide and inform experiments in the context of robust design.

5.2. Process map construction for AM design

In materials design, process maps have also been constructed to further accelerate and expedite development by providing valuable insight into PSPP trends of alloy system. Fig. 14 illustrates process maps for the additively manufactured Ni $_{50.3}$ Ti $_{29.2}$ Hf $_{20}$ system by LPBF with an incremental hatch spacing of 30 μ m, 60 μ m, and 90 μ m, from which several observations can be made:

• First, for all hatch space values, there is an increase in M_s with increasing power and velocity, corresponding to the keyholing print region. This culminates in a Ni- M_s insensitive region where additional Ni loss does not increase M_s beyond 306 °C. Conversely, as power and velocity decrease, there is a corresponding

decrease in M_s . A region with M_s of approximately 101.9 °C, corresponding to the M_s of the initial powder composition, is also observed once power and velocity combinations are low enough. This region is a result of the assumption which states that evaporation is negligible below the boiling temperature, where although these specific combinations of laser power and laser velocity could result in temperatures exceeding the melting point of the alloy system, this does not result in the evaporation of Ni from the melt pool or a change in M_s from the initial composition.

- Second, as the hatch spacing increases, the process region corresponding to the peak M_s is shown to diminish. This trend aligns with expectations that increasing hatch spacing results in the reduced magnitude of thermal events during the AM process, resulting in less evaporation, higher Ni content, and lower M_s than process parameters with lower hatch spacing and the same power and velocity values.
- Third, as the hatch spacing increases, the processing window to achieve a specific range of M_s increases. This translates to an increased tailorability of M_s for the design of components when utilizing larger hatch space values, in contrast to an increased sensitivity of M_s with power and velocity at smaller hatch space values. If a larger hatch spacing can be used in combination with multiple layer scans, a dramatic increase in the robustness of tailored location-specific properties can be achieved. When combined with printability maps depicting the relationship between process parameters and print quality (good, keyholing, balling, lack of fusion), the design space can be further constrained for the accelerated development and cost-effective design of defect-free components with location-specific properties [8,51].

6. Summary and conclusion

The complex physics of AM processes give rise to numerous challenges in material development and design. Not only is it necessary to accurately resolve the forward modeling problem of linking process parameters to properties for accelerated development, but a measure of confidence in model predictions is required for robust design. The forward model framework can then be leveraged for the inverse design of AM components with tailored location-specific properties. In this study, a fast-acting ICME framework was developed to predict locationspecific properties based on process parameters for Ni_{50.3}Ti_{29.7}Hf₂₀ SMAs manufactured by LPBF. Model components were calibrated and the framework validated with experiments, demonstrating good agreement between model predictions and experimentally measured M_s with an RMSE of 28.9 °C, a MAPE of 8.2%, and a Pearson correlation of 0.83. Furthermore, the viability of this modeling framework as a tool to inform and guide experiments for accelerated and robust design is supported by the 95% CIs determined through uncertainty quantification. In this regard, after accounting for the limitation on peak M_s value as determined through the empirical Ni- M_s relationship, 100% of the measured SHT M_s values for the Ni_{50.3}Ti_{29.7}Hf₂₀ cuboid specimens fell within the 2σ or 95% CIs of the framework predictions. Model predictions for measurements which exceeded the peak M_s could be improved upon through an improved empirical Ni- M_s relationship, however predictions are still within 20 °C of measurements and align with expected Ni-M_s trends. Additionally, the total framework uncertainty of predicted values fall within a tighter window than the uncertainty of standard composition measurement techniques such as WDS and ICP-AES. With confidence through validation and uncertainty quantification, the ICME framework is then leveraged to develop

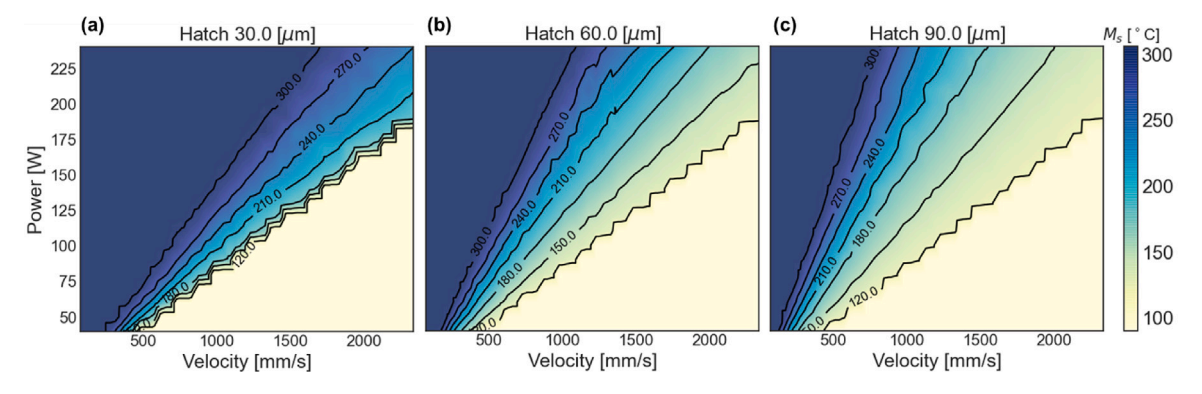


Fig. 14. Process maps for $Ni_{50.3}$ Ti_{29.7}Hf₂₀ SMAs manufactured by LPBF as predicted by the calibrated ICME framework for several hatch spacing values: (a) 30 μm, (b) 60 μm, (c) 90 μm. Laser velocity and laser power bounds are also selected based on experimental conditions. The associated M_s [°C] value is represented by the color scale, ranging from 101.9 [°C] (light) to 306 [°C] (dark).

process maps providing further insight into PSPP relationships across design space and to aid in cost-effective material development. M_s trends as a function of hatch spacing indicate an increased robustness of the design space with increased hath spacing. This can be exploited for the fabrication of tailored AM components with location-specific properties by leveraging printability maps in combination with multiple remelts of a single-layer to reduce the design space and maintain the larger M_s processing window provided by an increased hatch spacing.

In order to investigate the most impactful elements of this model chain, it would be necessary to carry out an in-depth sensitivity analysis. While this is out of the scope of the present contribution, one can surmise that the most impactful stage of the modeling chain is the evaporation model, given the extreme sensitivity of the transformation temperature to Ni amount. Of all the factors that control Ni evaporation, we are most uncertain about the Ni activity in the NiTi melt, as this quantity has never been measured for this system and in the CALPHAD model results from fits of the Gibbs energy of the liquid phase against phase diagram data. In future work, a more indepth investigation could be used to elucidate, in unambiguous terms, the most impactful uncertainty source in this framework.

CRediT authorship contribution statement

Meelad Ranaiefar: Methodology, Software, Formal analysis, Validation, Visualization, Writing – original draft, Writing – review & editing. Pejman Honarmandi: Software, Formal analysis, Writing – original draft, Writing – review & editing. Jiahui Ye: Software, Formal analysis, Writing – original draft. Chen Zhang: Investigation, Writing – original draft. Lei Xue: Investigation, Writing – original draft. Alaa Elwany: Supervision, Funding acquisition, Writing – review & editing. Ibrahim Karaman: Supervision, Funding acquisition, Writing – review & editing. Raymundo Arróyave: Conceptualization, Supervision, Funding acquisition, Writing – review & editing. Raymundo Arróyave: & editing.

Declaration of competing interest

The authors declare the following financial interests/personal relationships which may be considered as potential competing interests: The authors would like to acknowledge the support of AFRL through the AFRL/TAMU Data-Enabled Discovery and Design of Materials (D3EM) MLP program, under subcontractNo. UTC-165852-19F5830-19-02-C1 and Texas A&M High Performance Research Computing. PH acknowledges support from the National Science Foundation (NSF) through grant No. 1849085. AE acknowledges support from NSF grant No. 1846676. MR and RA acknowledge NSF through Grant No. 1545403.

Data availability

Data will be made available on request.

Acknowledgments

The authors would like to acknowledge the support of AFRL through the AFRL/TAMU Data-Enabled Discovery and Design of Materials (D³EM) MLP program, under subcontract No. UTC-165852-19F5830-19-02-C1. PH acknowledges support from the National Science Foundation (NSF) through Grant No. 1849085. AE acknowledges support from NSF Grant No. 1846676. MR and RA acknowledge NSF through Grant No. 1545403 (NRT-DESE: Data-Enabled Discovery and Design of Energy Materials). Portions of this research were conducted with the advanced computing resources provided by Texas A&M High Performance Research Computing.

References

- J. Ma, I. Karaman, R.D. Noebe, High temperature shape memory alloys, Int. Mater. Rev. 55 (5) (2010) 257–315.
- [2] R. Santamarta, R. Arróyave, J. Pons, A. Evirgen, I. Karaman, H. Karaca, R. Noebe, TEM study of structural and microstructural characteristics of a precipitate phase in Ni-rich Ni-Ti-Hf and Ni-Ti-Zr shape memory alloys, Acta Mater. 61 (16) (2013) 6191-6206.
- [3] J. Frenzel, E.P. George, A. Dlouhy, C. Somsen, M.-X. Wagner, G. Eggeler, Influence of Ni on martensitic phase transformations in NiTi shape memory alloys, Acta Mater. 58 (9) (2010) 3444–3458.
- [4] H. Karaca, E. Acar, H. Tobe, S. Saghaian, NiTiHf-based shape memory alloys, Mater. Sci. Technol. 30 (13) (2014) 1530–1544.
- [5] H. Sehitoglu, Y. Wu, L. Patriarca, G. Li, A. Ojha, S. Zhang, Y. Chumlyakov, M. Nishida, Superelasticity and shape memory behavior of NiTiHf alloys, Shape Mem. Superelasticity 3 (2) (2017) 168–187.
- [6] T. Umale, D. Salas, B. Tomes, R. Arroyave, I. Karaman, The effects of wide range of compositional changes on the martensitic transformation characteristics of NiTiHf shape memory alloys, Scr. Mater. 161 (2019) 78–83.
- [7] M. Ranaiefar, P. Honarmandi, L. Xue, C. Zhang, A. Elwany, I. Karaman, E. Schwalbach, R. Arroyave, A differential evaporation model to predict chemistry change of additively manufactured metals, Mater. Des. 213 (2022) 110328.
- [8] C. Zhang, L. Xue, S.A. Pestka, M. Ranaiefar, K.C. Atli, P. Honarmandi, R. Arróyave, I. Karaman, A. Elwany, Processing parameters and martensitic phase transformation relationships in near defect-free additively manufactured NiTiHf high temperature shape memory alloys, Mater. Des. 222 (2022) 110988.
- [9] P. Honarmandi, R. Arróyave, Uncertainty quantification and propagation in computational materials science and simulation-assisted materials design, Integr. Mater. Manuf. Innov. 9 (1) (2020) 103–143, http://dx.doi.org/10.1007/s40192-020-00168-2.
- [10] P. Honarmandi, R. Seede, L. Xue, D. Shoukr, P. Morcos, B. Zhang, C. Zhang, A. Elwany, I. Karaman, R. Arroyave, A rigorous test and improvement of the Eagar-Tsai model for melt pool characteristics in laser powder bed fusion additive manufacturing, Addit. Manuf. 47 (2021) 102300, http://dx.doi.org/10.1016/j.addma.2021.102300.
- [11] P. Honarmandi, M. Hossain, R. Arroyave, T. Baxevanis, A top-down characterization of NiTi single-crystal inelastic properties within confidence bounds through Bayesian inference, Shape Mem. Superelasticity 7 (1) (2021) 50–64.

- [12] V. Attari, P. Honarmandi, T. Duong, D.J. Sauceda, D. Allaire, R. Arroyave, Uncertainty propagation in a multiscale CALPHAD-reinforced elastochemical phase-field model, Acta Mater. 183 (2020) 452–470.
- [13] P. Honarmandi, L. Johnson, R. Arroyave, Bayesian probabilistic prediction of precipitation behavior in Ni-Ti shape memory alloys, Comput. Mater. Sci. 172 (2020) 109334.
- [14] P. Honarmandi, T.C. Duong, S.F. Ghoreishi, D. Allaire, R. Arroyave, Bayesian uncertainty quantification and information fusion in CALPHAD-based thermodynamic modeling, Acta Mater. 164 (2019) 636–647.
- [15] P. Honarmandi, N.H. Paulson, R. Arróyave, M. Stan, Uncertainty quantification and propagation in CALPHAD modeling, Modelling Simul. Mater. Sci. Eng. 27 (3) (2019) 034003.
- [16] P. Honarmandi, A. Solomou, R. Arroyave, D. Lagoudas, Uncertainty quantification of the parameters and predictions of a phenomenological constitutive model for thermally induced phase transformation in Ni–Ti shape memory alloys, Modelling Simul. Mater. Sci. Eng. 27 (3) (2019) 034001.
- [17] N.H. Paulson, E. Jennings, M. Stan, Bayesian strategies for uncertainty quantification of the thermodynamic properties of materials, Internat. J. Engrg. Sci. 142 (2019) 74–93.
- [18] P. Honarmandi, R. Arroyave, Using Bayesian framework to calibrate a physically based model describing strain-stress behavior of TRIP steels, Comput. Mater. Sci. 129 (2017) 66–81.
- [19] R.A. Otis, Z.-K. Liu, High-throughput thermodynamic modeling and uncertainty quantification for ICME, JOM 69 (5) (2017) 886–892.
- [20] R.E. Jones, F. Rizzi, B. Boyce, J.A. Templeton, J. Ostien, Plasticity Models of Material Variability Based on Uncertainty Quantification Techniques, Tech. Rep., Sandia National Lab.(SNL-NM), Albuquerque, NM (United States), 2017.
- [21] T.C. Duong, R.E. Hackenberg, A. Landa, P. Honarmandi, A. Talapatra, H.M. Volz, A. Llobet, A.I. Smith, G. King, S. Bajaj, et al., Revisiting thermodynamics and kinetic diffusivities of uranium–niobium with Bayesian uncertainty analysis, CALPHAD 55 (2016) 219–230.
- [22] F. Rizzi, R. Jones, B. Debusschere, O. Knio, Uncertainty quantification in MD simulations of concentration driven ionic flow through a silica nanopore. I. Sensitivity to physical parameters of the pore, J. Chem. Phys. 138 (19) (2013) 104104
- [23] M.C. Kennedy, A. O'Hagan, Bayesian calibration of computer models, J. R. Stat. Soc. Ser. B Stat. Methodol. 63 (3) (2001) 425–464.
- [24] M. Mahmoudi, G. Tapia, K. Karayagiz, B. Franco, J. Ma, R. Arroyave, I. Karaman, A. Elwany, Multivariate calibration and experimental validation of a 3D finite element thermal model for laser powder bed fusion metal additive manufacturing, Integr. Mater. Manuf. Innov. 7 (3) (2018) 116–135.
- [25] G. Tapia, L. Johnson, B. Franco, K. Karayagiz, J. Ma, R. Arroyave, I. Karaman, A. Elwany, Bayesian calibration and uncertainty quantification for a physics-based precipitation model of nickel-titanium shape-memory alloys, J. Manuf. Sci. Eng. 139 (7) (2017)
- [26] E.J. Schwalbach, S.P. Donegan, M.G. Chapman, K.J. Chaput, M.A. Groeber, A discrete source model of powder bed fusion additive manufacturing thermal history, Addit. Manuf. 25 (2019) 485–498, http://dx.doi.org/10.1016/j.addma. 2018 12 004
- [27] G.G. Gladush, I. Smurov, Physics of Laser Materials Processing: Theory and Experiment, Vol. 146, Springer Science & Business Media, Berlin, 2011.
- [28] J. Goldak, A. Chakravarti, M. Bibby, A new finite element model for welding heat sources, Metall. Trans. B 15 (2) (1984) 299–305.
- [29] W.E. King, H.D. Barth, V.M. Castillo, G.F. Gallegos, J.W. Gibbs, D.E. Hahn, C. Kamath, A.M. Rubenchik, Observation of keyhole-mode laser melting in laser powder-bed fusion additive manufacturing, J. Mater Process. Technol. 214 (12) (2014) 2915–2925, http://dx.doi.org/10.1016/j.jmatprotec.2014.06.005.

- [30] B. Zhang, R. Seede, L. Xue, K.C. Atli, C. Zhang, A. Whitt, I. Karaman, R. Arroyave, A. Elwany, An efficient framework for printability assessment in laser powder bed fusion metal additive manufacturing, Addit. Manuf. 46 (2021) 102018.
- [31] L. Murr, Computer simulation in materials science and engineering, in: Handbook of Materials Structures, Properties, Processing and Performance, Springer, Cham, 2015, pp. 1105–1121, http://dx.doi.org/10.1007/978-3-319-01905-5.
- [32] U. Von Toussaint, Bayesian inference in physics, Rev. Modern Phys. 83 (3) (2011) 943–999, http://dx.doi.org/10.1103/RevModPhys.83.943.
- [33] S.M. Lynch, Introduction To Applied Bayesian Statistics and Estimation for Social Scientists, Springer Science & Business Media, Berlin, 2007.
- [34] A. Gelman, J.B. Carlin, H.S. Stern, D.B. Rubin, Bayesian Data Analysis, Chapman and Hall/CRC, Cambridge, 1995.
- [35] D. Foreman-Mackey, D.W. Hogg, D. Lang, J. Goodman, Emcee: The MCMC hammer, Publ. Astron. Soc. Pac. 125 (925) (2013) 306–312, http://dx.doi.org/ 10.1086/670067.
- [36] S.-K. Au, Connecting Bayesian and frequentist quantification of parameter uncertainty in system identification, Mech. Syst. Signal Process. 29 (2012) 328–342, http://dx.doi.org/10.1016/j.ymssp.2012.01.010.
- [37] M. Laine, GitHub, 2018, URL https://github.com/mjlaine/mcmcstat.
- [38] H. Haario, M. Laine, A. Mira, E. Saksman, DRAM: Efficient adaptive MCMC, Stat. Comput. 16 (4) (2006) 339–354, http://dx.doi.org/10.1007/s11222-006-9438-0.
- [39] H. Haario, E. Saksman, J. Tamminen, An adaptive metropolis algorithm, Bernoulli 7 (2) (2001) 223–242, http://dx.doi.org/10.2307/3318737.
- [40] S.P. Donegan, E.J. Schwalbach, M.A. Groeber, Zoning additive manufacturing process histories using unsupervised machine learning, Mater. Charact. 161 (2020) 110123.
- [41] S. Dushman, Scientific Foundations of Vacuum Technique, John Wiley and Sons, Inc., 1949.
- [42] C. Yaws, The Yaws Handbook of Vapor Pressure: Antoine Coefficients, Gulf Professional Publishing, 2015.
- [43] X. He, T. DebRoy, P. Fuerschbach, Alloying element vaporization during laser spot welding of stainless steel, J. Phys. D: Appl. Phys. 36 (23) (2003) 3079.
- [44] O. Benafan, G. Bigelow, D. Scheiman, Transformation behavior in NiTi-20Hf shape memory alloys-transformation temperatures and hardness, Scr. Mater. 146 (2018) 251–254.
- [45] X. Wang, K. Putyera, Accurate determination of the chemical composition of nickel-titanium binary alloys by NIST high performance inductively coupled plasma – optical emission spectroscopy method, in: Shape Memory and Superelastic Technologies Conference, SMST, 2015.
- [46] M. Nematollahi, G. Toker, S. Saghaian, J. Salazar, M. Mahtabi, O. Benafan, H. Karaca, M. Elahinia, Additive manufacturing of Ni-rich NiTiHf20: Manufacturability, composition, density, and transformation behavior, Shape Mem. Superelasticity 5 (1) (2019) 113–124.
- [47] G.P. Toker, M. Nematollahi, S.E. Saghaian, K.S. Baghbaderani, O. Benafan, M. Elahinia, H.E. Karaca, Shape memory behavior of NiTiHf alloys fabricated by selective laser melting, Scr. Mater. 178 (2020) 361–365.
- [48] F. Pedregosa, G. Varoquaux, A. Gramfort, V. Michel, B. Thirion, O. Grisel, M. Blondel, P. Prettenhofer, R. Weiss, V. Dubourg, J. Vanderplas, A. Passos, D. Cournapeau, M. Brucher, M. Perrot, E. Duchesnay, Scikit-learn: Machine learning in Python, J. Mach. Learn. Res. 12 (2011) 2825–2830.
- [49] J. Salvatier, T.V. Wiecki, C. Fonnesbeck, Probabilistic programming in Python using PyMC3, PeerJ Comput. Sci. 2 (2016) e55.
- [50] O. Benafan, G. Bigelow, A. Garg, R. Noebe, D. Gaydosh, R. Rogers, Processing and scalability of NiTiHf high-temperature shape memory alloys, Shape Mem. Superplasticity (2021) 1–57
- [51] S. Sheikh, M. Ranaiefar, P. Honarmandi, B. Vela, P. Morcos, D. Shoukr, I. Karaman, A. Elwany, R. Arroyave, An automated fully-computational framework to construct printability maps for additively manufactured metal alloys., 2022, http://dx.doi.org/10.2139/ssrn.4290450, Available at SSRN: 4290450.